PAPER • OPEN ACCESS

Experimental benchmark data for Monte Carlo simulated radiation effects of gold nanoparticles. Part I: Experiment and raw data analysis

View the article online for updates and enhancements.

Physica Scripta

Experimental benchmark data for Monte Carlo simulated radiation effects of gold nanoparticles. Part I: Experiment and raw data analysis

Hans Rabus[1] , Philine Hepperle[1,2], Christoph Schlueter[3], Andrei Hloskovsky[3] and Woon Yong Baek[1]

1 Physikalisch-Technische Bundesanstalt, Braunschweig and Berlin, Germany
2 Leibniz Universität Hannover, Institute of Radioecology and Radiation Protection, Hannover, Germany
3 Deutsches Elektronen-Synchrotron DESY, Hamburg, Germany
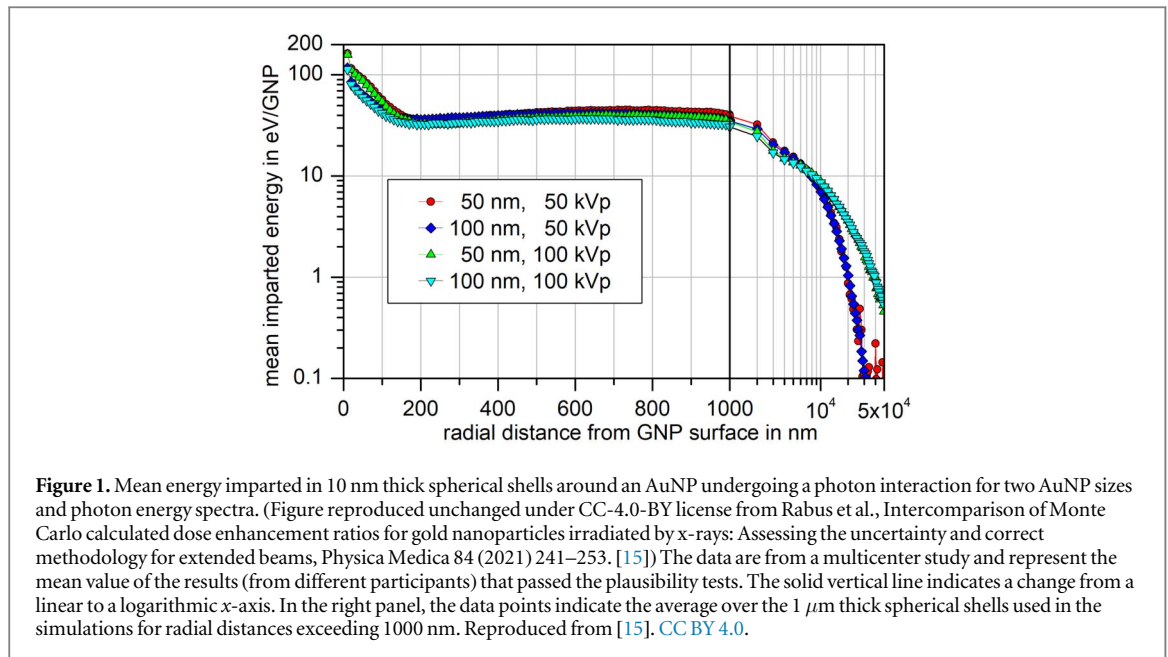
E-mail: hans.rabus@ptb.de

Abstract

Electron emission spectra of gold nanoparticles (AuNPs) after photon interaction were measured over the energy range between 50 eV and 9500 eV to provide reference data for Monte Carlo radiation-transport simulations. Experiments were performed with the HAXPES spectrometer at the PETRA III high-brilliance beamline P22 at DESY (Hamburg, Germany) for photon energies below and above each of the gold L-edges, that is, at 11.9 keV, 12.0 keV, 13.7 keV, 13.8 keV, 14.3 keV, and 14.4 keV. The study focused on a sample with gold nanoparticles with an average diameter of 11.0 nm on a thin carbon foil. Additional measurements were performed on a sample with 5.3 nm gold nanoparticles and on reference samples of gold and carbon foils. Further measurements were made to calibrate the photon flux monitor, to characterize the transmission function of the electron spectrometer, and to determine the size of the photon beam. This allowed the determination of the absolute values of the spectral particle radiance of secondary electrons per incident photon flux. The paper presents the experimental and raw data analysis procedures, reviews the data obtained for the nanoparticle samples, and discusses their limitations.

1. Introduction

Gold nanoparticles (AuNPs) are considered potential radiosensitizers for radiation therapy [1–6]. AuNPs have been shown to increase the biological effectiveness of ionizing radiation *in vitro* and *in vivo* [5–9]. In these studies, the increase in average absorbed dose resulting from the higher absorption of radiation by the high-Z material gold (Au), as compared to biological matter or water, was much smaller than the observed effects. Therefore, these effects are often attributed to a local dose enhancement due to low-energy electrons from Auger cascades following core–shell ionizations of gold atoms [10–12]. Since this local enhancement is limited to microscopic dimensions in the range of a few 100 nm [10–15], it is often assessed by numerical simulations using radiation-transport Monte Carlo (MC) codes. The results from such MC simulations often show a wide range of outcomes between different studies [16, 17]. However, a recent comparison exercise [18, 19] demonstrated that some of the confusion in the literature is due to conceptional misunderstandings [13–15] or to a lack of quality assurance of simulation results [20, 21].

Benchmarking MC simulations of the dosimetric effects of AuNPs with experimental data is challenging. Previous experimental studies were moreover limited to determining the macroscopic average dose increase [22–24]. In addition, the measurement of locally enhanced dose in the vicinity of AuNPs is not yet possible for two reasons. The first reason is that the range of dose enhancement is limited to microscopic dimensions. And the second one is the low probability of photon interaction in an AuNP, which implies that only a small fraction of AuNPs contributes to the dose enhancement.

Figure 1. Mean energy imparted in 10 nm thick spherical shells around an AuNP undergoing a photon interaction for two AuNP sizes and photon energy spectra. (Figure reproduced unchanged under CC-4.0-BY license from Rabus et al., Intercomparison of Monte Carlo calculated dose enhancement ratios for gold nanoparticles irradiated by x-rays: Assessing the uncertainty and correct methodology for extended beams, Physica Medica 84 (2021) 241–253. [15]) The data are from a multicenter study and represent the mean value of the results (from different participants) that passed the plausibility tests. The solid vertical line indicates a change from a linear to a logarithmic *x*-axis. In the right panel, the data points indicate the average over the 1 μm thick spherical shells used in the simulations for radial distances exceeding 1000 nm. Reproduced from [15]. CC BY 4.0.

The expected number $\bar{n}_p$ of photon interactions in an AuNP is proportional to the absorbed dose D and to the volume of the AuNP or the third power of its diameter, d_g [13, 20], and can be estimated by

$$\bar{n}_p = C_D \times d_g{}^3 \times D \tag{1}$$

The proportionality constant, C_D, depends on the photon energy spectrum. For the 50 kVp and 100 kVp x-ray spectra considered in above comparison exercise [18, 19], C_D is about 3.6×10^{-7} Gy^{-1} nm^{-3} and 2.7×10^{-7} Gy^{-1} nm^{-3}, respectively.

Therefore, the expected number of photon interactions in a 13 nm AuNP is about 8×10^{-4} and 6×10^{-4}, respectively, for a dose of 1 Gy. According to Dou *et al* [25], diameters of about 13 nm may be optimal for clinical theranostic applications of AuNPs. Most radiobiological studies reviewed by Kuncic and Lacombe [6] used AuNP sizes well below 20 nm, that is, much smaller than the 50 nm and 100 nm considered in the MC comparison exercise.

The dosimetric effects of AuNPs result from electrons emitted after a photon interaction in the AuNPs. This is illustrated in figure 1, which shows the energy imparted by these electrons in radial water shells around the 50 nm and 100 nm AuNPs considered in the exercise. The energy imparted decreases rapidly within the first 150 nm from the AuNP. This is due to electrons with energies below about 3.5 keV being stopped, namely Auger electrons from the M and N-shells of Au, Coster-Kronig electrons from the L-shells of Au, and low-energy secondary electrons produced in the AuNP.

The plateau between 150 nm and 1000 nm is due to L-shell Auger electrons, for which a range in water between about 1.5 μm and 3 μm can be estimated from the ESTAR database [26]. The long-range energy deposition shown in the right panel of figure 1 is due to photoelectrons and Compton electrons leaving the AuNP.

The data shown in the left panel of figure 1 suggest that M-shell Auger electrons and the other low-energy electrons can contribute to the biological effects only when the AuNPs are located in the cell nucleus (which is generally not observed [27]) or near the nucleus' membrane in the cytoplasm. In contrast, AuNPs from a much larger volume of the cytoplasm can contribute to the biological effects via emitted L-shell Auger electrons.

In the MC comparison exercise, the largest differences between simulations performed with different codes were seen in the ancillary results for the energy spectra of emitted electrons [18, 19], especially at low energies. Discrepancies remained for some results after all necessary corrections were made to the originally reported ones [20]. A major reason for these remaining discrepancies was that one code used a newly developed dataset of cross sections for electron interactions in gold at energies down to the ionization threshold, which was derived from theoretical models [28]. Most other codes either used empirical extrapolations of the cross-section data from the Livermore database to lower energies or used the energy cut-offs implied by the energy ranges of that database. Recently, cross-sections for electron transport at low energies in gold have also become available in the Geant4-DNA code system [29, 30].

The present project was initiated with the goal of providing an experimental dataset of electron emissions from gold nanoparticles as a benchmark for MC simulations, and thus indirectly, for the electron cross-section
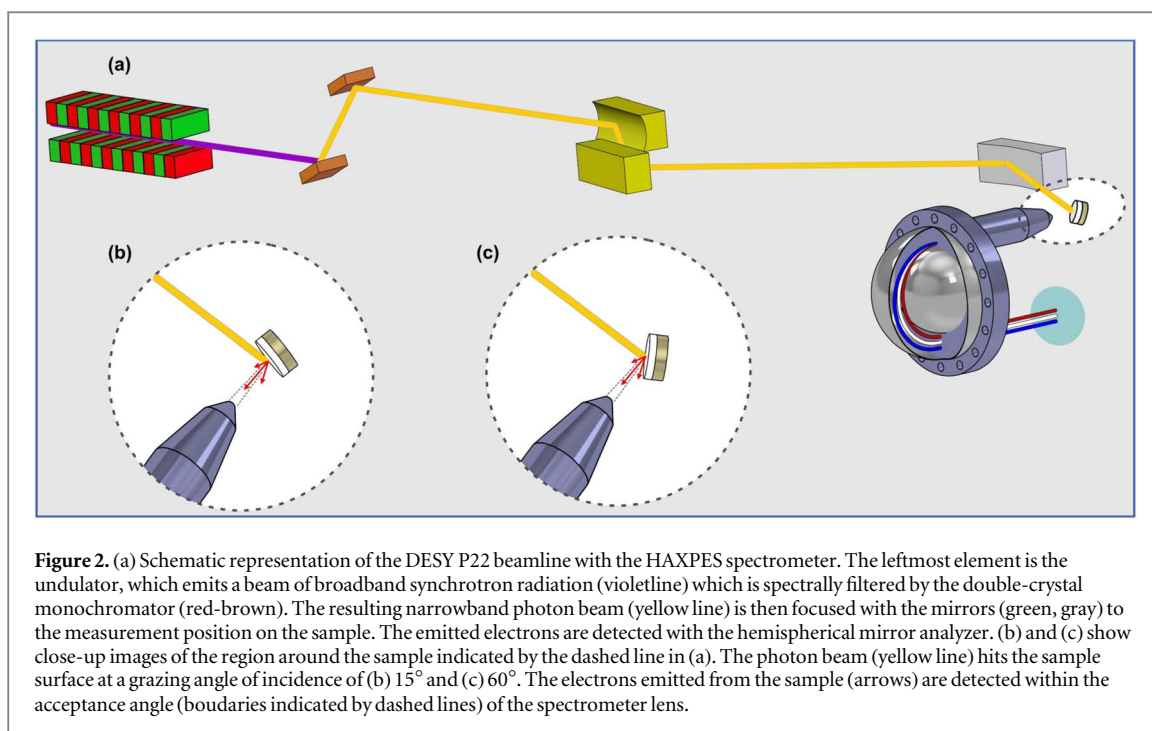
Figure 2. (a) Schematic representation of the DESY P22 beamline with the HAXPES spectrometer. The leftmost element is the undulator, which emits a beam of broadband synchrotron radiation (violetline) which is spectrally filtered by the double-crystal monochromator (red-brown). The resulting narrowband photon beam (yellow line) is then focused with the mirrors (green, gray) to the measurement position on the sample. The emitted electrons are detected with the hemispherical mirror analyzer. (b) and (c) show close-up images of the region around the sample indicated by the dashed line in (a). The photon beam (yellow line) hits the sample surface at a grazing angle of incidence of (b) 15° and (c) 60°. The electrons emitted from the sample (arrows) are detected within the acceptance angle (boudaries indicated by dashed lines) of the spectrometer lens.

datasets implemented in the MC codes. Due to the relevance described above, the focus was placed on the energy range of Au L-shell Auger electrons and below.

Electron spectrometers require the samples under investigation to be in an ultra-high vacuum environment. Electron spectra emitted from AuNPs in vacuum should be very similar to those emitted from AuNPs in water, the only difference being that electrons may be emitted twice after backscattering in the water surrounding the AuNP. This is expected to be a negligible effect.

The low photon interaction probability in AuNPs makes such experiments challenging as high photon flux rates are required to achieve a reasonable signal-to-noise ratio. Therefore, the experiments were conducted in a synchrotron radiation facility. The beams used had photon fluence rates between $1 \times 10^{16}\,\mathrm{cm}^{-2}\,\mathrm{s}^{-1}$ and $5 \times 10^{16}\,\mathrm{cm}^{-2}\,\mathrm{s}^{-1}$, corresponding to absorbed dose rates to water between 230 kGy/s and 40 kGy/s. To further optimize the signal-to-noise ratio and to investigate the contributions of the Auger cascades from the different Au L-shells, the photon energies were chosen slightly above and slightly below each of the corresponding binding energies.

Smaller sizes of roughly 5 nm and 10 nm were used instead of AuNPs with the sizes considered in the code comparison exercise. These sizes of nanoparticles were used in the studies of Kim *et al* [31] and Hainfeld *et al* [32] and also in ongoing research by collaborating radiobiology groups at the radiooncology department of the University Medical Center Hamburg-Eppendorf (Hamburg, Germany) and Université de Namur (Namur, Belgium), which provided the AuNPs used in this study. According to Dou *et al* [25], these AuNP sizes appear to be more clinically relevant than smaller or larger particles.

In this first part of the paper, the experimental procedures and data analysis methodology are described, with the emphasis on obtaining absolute results. The second part of the paper deals with the comparison of the measured data for a thin gold foil with MC simulations [33]. In the third part of the paper, the measured data will be used for benchmarking the 'radial' code [34]. The detailed line shape analysis of the results on AuNP samples and a comparison with simulations will be presented in the fourth part.

This work contains three supplements describing auxiliary experiments and data analyses to characterize the experimental setup, which allowed the determination of results on an absolute scale. A fourth supplement shows additional results from measurements on the samples studied. The figures and tables in these supplements are referred to with the suffix 'Sx-' before the figure or table number, where 'x' is the supplement number.

2. Materials and methods

2.1. Experimental setup

The experimental setup is schematically schown in figure 2. The measurements were performed at the high-brilliance beamline P22 of PETRA III at DESY (Hamburg, Germany), which offers photon energies between 2.4 keV and 15 keV at a photon flux in the order of $10^{13}\,\mathrm{s}^{-1}$ and is equipped with a high-resolution hard x-ray

Figure 3. Photographs of an aluminum support covered with a 50 nm thick self-supporting carbon foil mounted on a wedge-shaped DESY copper sample holder. In the top view on the left, the dark spot in the center of the left aperture is an AuNP sample deposited by the drop-casting method. The part of the carbon foil covering the right aperture was used for reference measurements.

Figure 4. Photographs of the other samples used in the measurements mounted on wedge-shaped copper DESY sample holders. Left: A 100 nm thick gold foil attached to an aluminum support with two 5 mm apertures. Right: The 5.3 nm AuNP sample provided by Université de Namur.

Table 1. Energy ranges and retarding ratios used in the electron spectra measurements. The energy step was always 1 eV. The retarding ratio for the first energy range was generally $R = 1$, except for the measurements of the gold foil, where $R = 10$ was used.

Energy range	Start energy/eV	End energy/eV	Retarding ratio R
1	50	120	1 (10)
2	100	1200	10
3	1000	3500	50
4	3500	6500	50
5	6000	9500	100

photoelectron spectroscopy (HAXPES) instrument that is capable of measuring electron energies up to 10 keV [35]. The undulator beam is monochromatized by an LN_2-cooled double crystal monochromator (DCM, red-brown items in figure 2(a)). For the present experiments, the Si(111) crystals of the monochromator were used, and the undulator was operated at its third harmonic.

The HAXPES electron spectrometer is a SPECS Phoibos 225 HV hemispherical analyzer (SPECS Surface Nano Analysis Ltd, Germany) mounted on an ultrahigh vacuum analysis chamber (base pressure $\sim 2 \times 10^{-9}$ mbar) such that its optical axis is horizontal and at right angles to the photon beam. The analysis chamber was equipped with a fully motorized 5-axis manipulator with three translational and two rotational degrees of freedom [35] and an attached load-lock chamber (average base pressure of $2 \cdot 10^{-9}$ mbar). Samples mounted on standard wedge-shaped copper sample holders manufactured at DESY (DESY, Germany) were introduced into the load-lock chamber and stored on a sample carousel. A long arm transfer allowed samples to be exchanged between the sample carousel and the manipulator in the analysis chamber.

To monitor the photon flux, the current of a photodiode detecting emitted electrons and scattered photons from a thin carbon foil that was placed in the beamline in front of the last focusing mirror was recorded with one of the channels of a four-channel digitizer.

2.2. Samples and sample preparation

The main samples to be investigated consisted of citrate-stabilized gold nanoparticles (AuNPs) coated with polyethylene glycol (PEG) 11-mercaptoundecanoic acid (MUA). They were manufactured by the University of Hamburg (Hamburg, Germany) and were provided by the Medical Center Hamburg-Eppendorf (UKE,

Hamburg, Germany). Their size distribution had a mean diameter of 11 nm and a standard deviation of 0.9 nm [36]. (Note that the value of 1.8 nm given in [36] is two standard deviations). The AuNP samples for the experiments were prepared on a 50 nm thick self-supporting carbon foil (specified mass per area 10 μg cm^{-2}, purity 99.997%) supplied by Goodfellow (Hamburg, Germany) on temporary glass supports.

The carbon foil was suspended over the 5 mm holes of a 1 mm thick aluminum support of rectangular shape and dimensions 22 mm × 13 mm, manufactured in a mechanical workshop of PTB (Braunschweig, Germany). The AuNP solution was stirred to homogenize the solution. A 0.5 μl drop of AuNP solution was cast onto the carbon microsheet in the center of one of the two holes in the sample holder using an Eppendorf® pipette. The drop was allowed to dry for 24 h at room temperature under ambient air.

AuNP samples prepared on carbon microsheets following the same protocol were examined by x-ray photoelectron spectroscopy (XPS) and scanning transmission electron microscope (STEM) to determine the size, shape, and surface coverage of the gold nanoparticles [36, 37]. The sample used in the measurements was examined by STEM after the beamtime.

For the experiments, the aluminum supports of the samples were attached with double-sided adhesive copper tape to standard wedge-shaped copper sample holders used at DESY (figure 3).

Two other samples were also used in the experiments (figure 4). One consisted of a 100 nm thick gold foil mounted on an aluminum support of the same type. The second sample consisted of nanoparticles with an average diameter of 5.3 nm coated with PEG. They were deposited by ion beam sputtering on a 100 nm thick carbon foil suspended on a cylindrical aluminum support with an outer diameter of 20 mm and a 5 mm aperture in the center. This sample was fabricated at the University of Namur (Namur, Belgium).

2.3. Performed measurements of electron spectra

Electron emission spectra of AuNP and reference samples were recorded for electron energies between 50 eV and 9.5 keV in 1 eV steps. The measurements were performed for six photon energies corresponding to values slightly below and above the gold L-edges (11.9 keV, 12.0 keV, 13.7 keV, 13.8 keV, 14.3 keV, 14.4 keV). To facilitate the correction of its energy-dependent transmission, the spectrometer was operated in a fixed retarding ratio mode. Different values for the retarding ratio were used in different energy ranges (table 1).

For the nanoparticle samples, data were recorded for two different grazing-incidence angles, namely 15° and 60°. A small grazing-incidence angle leads to a larger irradiated area and thus to a better signal-to-noise ratio. At the same time, the sensitivity to lateral movements of the photon beam increases. A 15° grazing-incidence angle is the commonly used optimal choice for a trade-off between the two effects.

At a small grazing angle of incidence, the scattering of emitted electrons by neighboring AuNPs in the surface plane is reduced. This scattering is best studied at normal incidence of the radiation, but then the surface seen by the spectrometer would disappear. An incidence angle of 60° is a good compromise between studying in-plane scattering and obtaining a reasonable signal.

For the gold and carbon foil samples, measurements were only taken at 15° grazing incidence, and for the carbon foil, only for the highest photon energy.

During the measurements, the count rate of the HAXPES and the current signal of the photon flux monitor were recorded simultaneously for each electron energy data point. To prevent the HAXPES electron detectors from overloading, the photon flux was reduced for some samples and energy ranges by moving attenuators that were installed upstream of the photon flux monitor into the beam.

Dark current suppression was repeatedly performed on the CAEN multi-channel electrometer used to measure the photon flux monitor signal. The remaining dark current was on the order of 10 pA and is treated as an uncertainty. The measured currents were on the order of several tens of nA (see table S1.1 in Supplement 1).

2.4. Data analysis

The data analysis was based on the following measurement equation for the spectral particle radiance per photon flux, $d^3\varepsilon/dA\,dE\,d\Omega$, of electrons emitted from the irradiated sample. When all electrons passing the energy analyzer are registered, $d^3\varepsilon/dA\,dE\,d\Omega$ is the number of emitted electrons per incident photon, per electron energy interval, per solid angle, and per surface area (averaged over the irradiated area):

$$\frac{d^3\varepsilon(E_e)}{dA\,dE\,d\Omega} = \frac{\dot{N}_m}{I_0 E_e} G(R_r,\,R) \frac{R}{R_r} \frac{Q_0(E_p)\,E_r}{T(E_{ar},\,R_r)} \frac{A_r}{A_b} \sin\theta \tag{2}$$

In equation (2), $\dot{N}_m$ is the measured count rate at the set energy E_e and the retarding ratio R of the electron spectrometer, I_0 is the measured current of the photon flux monitor, and Q_0 is the average detected charge per photon passing the photon flux monitor. E_r and R_r are reference values for the kinetic energy and the retarding ratio for which the spectrometer transmission T is known at the pass energy $E_{ar} = E_r/R_r$. A_r is the beam cross-sectional area used in electron ray tracing for determining the transmission, A_b is the actual beam cross-sectional area, and θ is the angle of grazing incidence of the photon beam on the sample surface. The factor $\sin\theta$ takes

into account that the surface area hit by the photon beam is increased by a factor of $1/\sin\theta$. The quantity G in equation (2) is the ratio of the spectrometer transmission at a reference pass energy E_{ar} and retarding ratio R_r to the one for retarding ratio R. Details on the determination of the photon flux, photon beam size, and spectrometer transmission function are given in Supplements 1, 2, and 3.

In a measurement run on a sample, five datasets of emitted electron spectra were recorded with the HAXPES spectrometer, using different retarding ratios R depending on the scanned energy ranges (table 1). To obtain a joint dataset, the individual datasets were first normalized to the photon flux monitor signal. This was done to remove the temporal variation of the photon flux. (It did not, however, remove the negligibly small glitches at storage ring top-ups due to differences between the HAXPES dwell time and the integration time of the CAEN used for measurement of the photon flux monitor current).

The data were then divided by the electron energy to compensate for the proportionality with E of the spectrometer transmission in the fixed retarding ratio mode. In the next step, for each pair of adjacent energy scans with retarding ratios R_1 and R_2, the ratios of the two measurements were calculated for all common energy points in the overlap region. Mean and standard deviation were used as an estimate and the uncertainty of the ratio $G(R_1, R_2)$. Appropriate combinations of these ratios were then used to calculate the $G(R_r, R)$ ratios in equation (2) for each scan range. After multiplying the data in each scan range by the respective factor $G(R_r, R)$, the datasets were merged. In the overlap intervals between successive energy ranges, the average values of the two scans were used. Finally, the merged dataset was multiplied by the overall calibration factor, this being the fraction given as last factor in equation (2), to obtain the spectral particle radiance of electrons per incident photon flux.

3. Results

3.1. Overview

To get a first impression of the measurement results, figure 5 shows the obtained electron energy spectra of the 11 nm AuNP samples for the two photon energies 11.9 keV and 14.4 keV. The first energy is slightly below the Au L_3 binding energy, so only electrons in the M and outer shells can be excited by photoabsorption.

The spectrum in figure 5(a) is dominated by the photoabsorption peaks of the M_1, M_2, and M_3-shells, which exhibit pronounced low-energy tailing. They are overlaid by a background consisting of the low-energy tailing of the M_4 and M_5 photoelectron lines, which peak at energies beyond the range studied here. In the energy range between 3 keV and 8 keV, this spectrum is generally characterized by the absence of spectral features, except for a sharp peak at about 7850 eV, which is the K-shell photoabsorption peak of potassium.

In the energy range between 0.8 keV and 2 keV, the spectrum contains the Auger electrons produced in non-radiative filling of vacancies in the M-shells. The large number of different transitions with energies close to each other results in a quasi-continuum, which has also been reported by other authors [38].
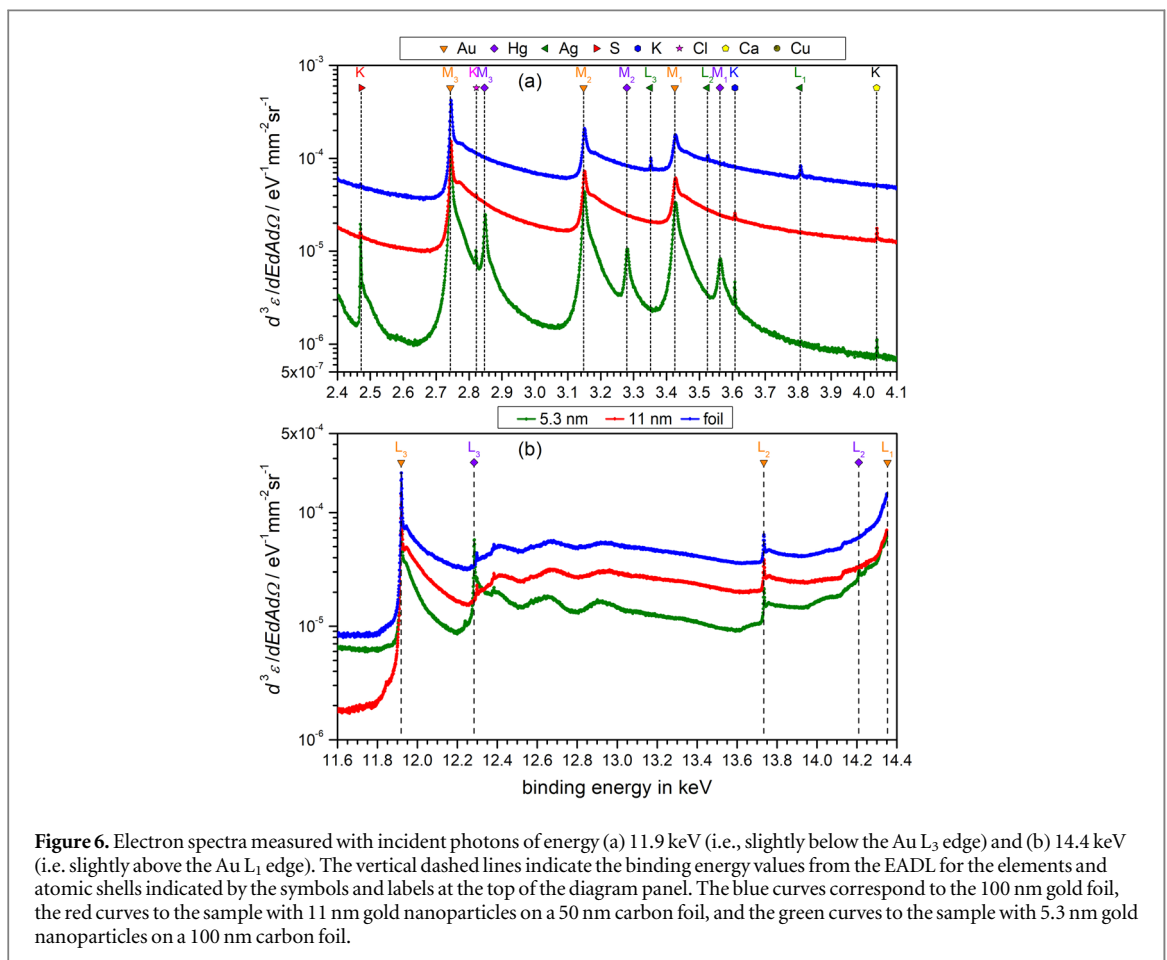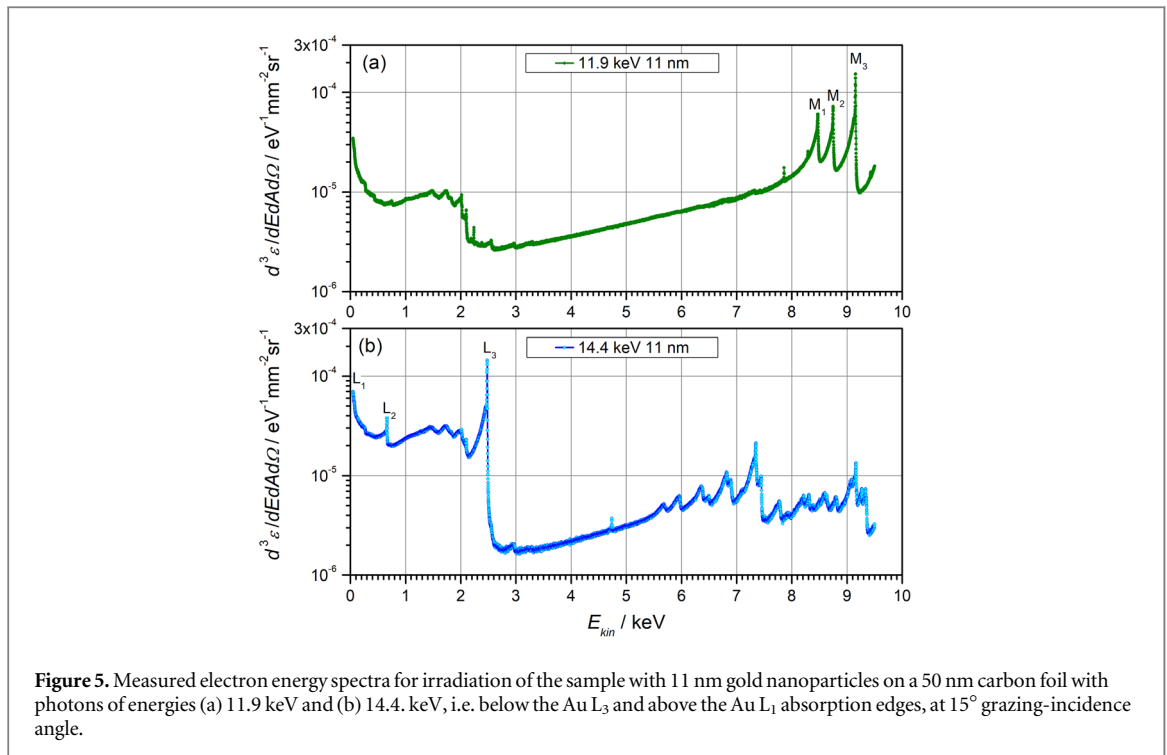
In the electron emission spectrum produced by 14.4 keV photons (blue symbols), a large number of lines can be seen in the energy range between 5.5 keV and 9.5 keV. Since the M-shell photoelectrons have shifted to higher energies outside the range covered by the measurements, these lines are due to Auger transitions when vacancies in the L-shells are filled. At this photon energy, all L-shells of gold can be excited, leading to the intense photoelectron peaks at about 0.8 keV (L_2) and 2.5 keV (L_3). (The L_1 line coincides with the low-energy secondary electron peak close to the lowest detected electron energy).

These peaks and their tails strongly overlap with the M-shell Auger electrons, highlighting the complexity of a quantitative line shape analysis in this energy range. Changes in the intensity of the M Auger lines are expected for the higher photon energy due to the enhanced production of M-shell Auger electrons in the de-excitation cascade following photoabsorption in the L-shells of gold. In addition, the Coster-Kronig electrons produced when an L-shell vacancy is filled by another electron from a higher L-shell are also expected to appear in this energy range [39].

It should be noted that the sharp peak at about 4.7 keV appearing at about 2.2 keV in the spectrum for 11.9 keV photons corresponds to the K-shell photoelectron of zinc. Like the potassium peak mentioned earlier, this suggests surface contamination from residues of the chemicals used in processing the gold nanoparticles during sample preparation. It is also worth noting that there is no evidence of a K-shell photopeak of Cu in the samples (which would appear at about 3 keV and 6.5 keV for 11.9 keV and 14.4 keV photons, respectively).
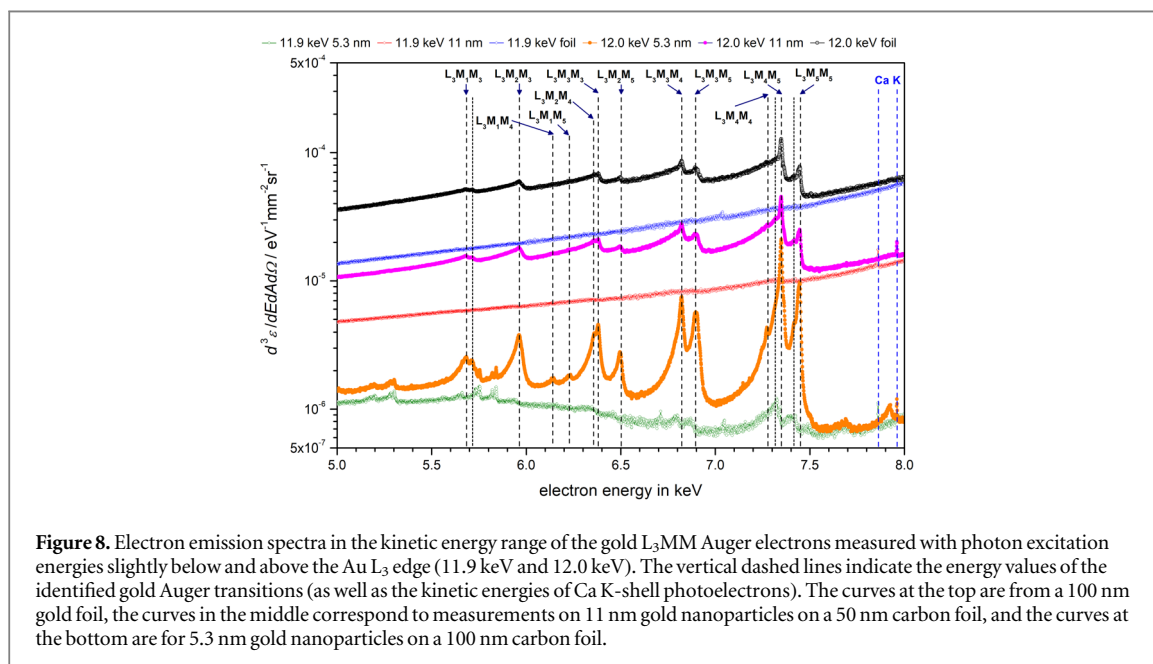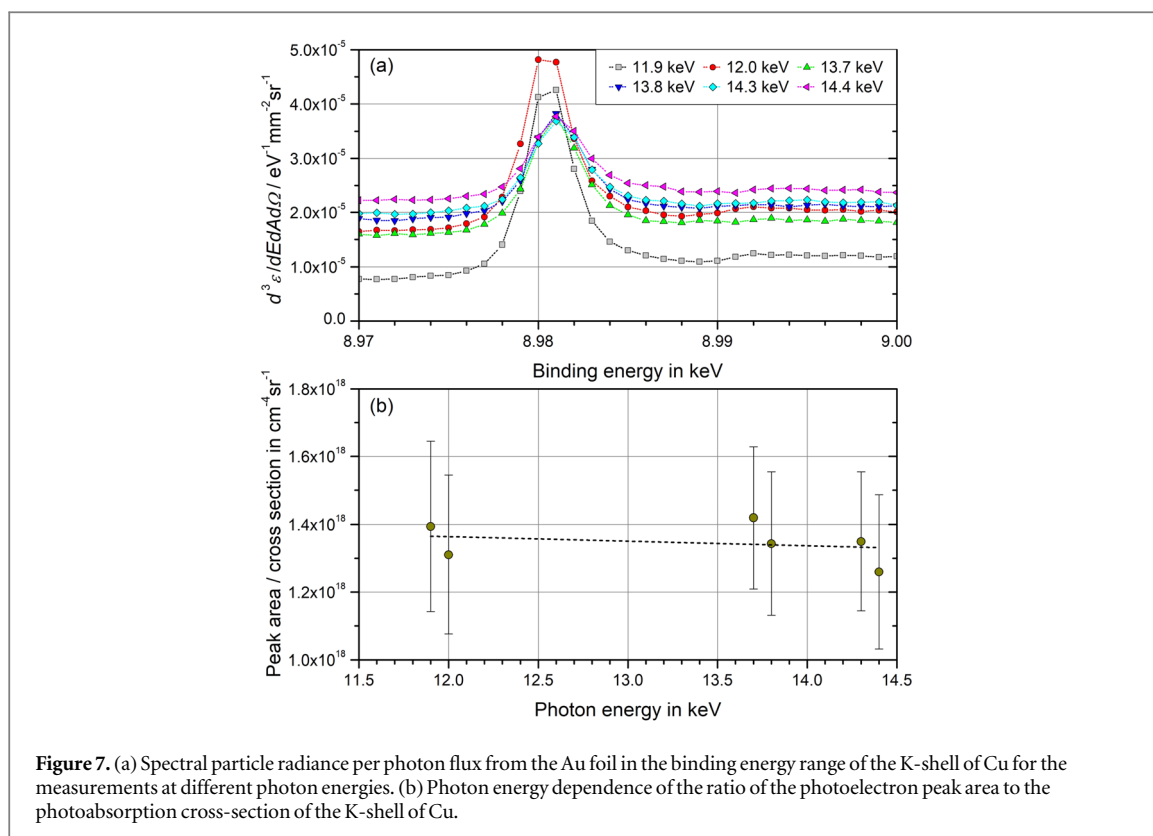
3.2. Photoelectron spectra

To further characterize the chemical composition of the AuNP and gold foil samples, figure 6 shows the emitted electron spectra produced by (a) 11.9 keV and (b) 14.4 keV photons as a function of binding energy in the energy ranges between 2.4 keV and 4.1 keV and between 11.6 keV and 14.4 keV, respectively. The vertical dashed lines

Figure 5. Measured electron energy spectra for irradiation of the sample with 11 nm gold nanoparticles on a 50 nm carbon foil with photons of energies (a) 11.9 keV and (b) 14.4. keV, i.e. below the Au L_3 and above the Au L_1 absorption edges, at 15° grazing-incidence angle.

Figure 6. Electron spectra measured with incident photons of energy (a) 11.9 keV (i.e., slightly below the Au L_3 edge) and (b) 14.4 keV (i.e. slightly above the Au L_1 edge). The vertical dashed lines indicate the binding energy values from the EADL for the elements and atomic shells indicated by the symbols and labels at the top of the diagram panel. The blue curves correspond to the 100 nm gold foil, the red curves to the sample with 11 nm gold nanoparticles on a 50 nm carbon foil, and the green curves to the sample with 5.3 nm gold nanoparticles on a 100 nm carbon foil.

show the binding energies of the atomic levels according to the evaluated atomic data library (EADL) [39, 40]. The element is coded by symbol type and color, and the atomic shell is indicated as a label above each symbol.

In addition to the photoelectron lines from the M-shells of gold, lines corresponding to several other elements can be identified in figure 6(a). The photoelectron peak from the K-shell of sulfur is expected for the

Figure 7. (a) Spectral particle radiance per photon flux from the Au foil in the binding energy range of the K-shell of Cu for the measurements at different photon energies. (b) Photon energy dependence of the ratio of the photoelectron peak area to the photoabsorption cross-section of the K-shell of Cu.

Figure 8. Electron emission spectra in the kinetic energy range of the gold L_3MM Auger electrons measured with photon excitation energies slightly below and above the Au L_3 edge (11.9 keV and 12.0 keV). The vertical dashed lines indicate the energy values of the identified gold Auger transitions (as well as the kinetic energies of Ca K-shell photoelectrons). The curves at the top are from a 100 nm gold foil, the curves in the middle correspond to measurements on 11 nm gold nanoparticles on a 50 nm carbon foil, and the curves at the bottom are for 5.3 nm gold nanoparticles on a 100 nm carbon foil.

nanoparticle samples due to the presence of a thiol group that binds the polymer passivation layer to the nanoparticle surface. On the logarithmic scale it appears more pronounced for the smaller nanoparticles, which have a higher proportion of surface atoms. The presence of photoelectron peaks of calcium, chlorine, and potassium is due to the chemicals used in the treatment of the samples. The gold foil shows significant contamination with silver and copper (figure 7(a)), which is due to the good alloyability of the three elements.

The observation of a significant signal of mercury (Hg) photoelectrons in the spectra of the 5.3 nm gold nanoparticles was a surprise. This contamination is attributed to potential impurities of the gold substrate used in the dry physical production process. Gold and mercury are also easily alloyed. Using the peak height with respect to the nearest minimum at higher energies and the photo-absorption cross-sections for the M_3, M_4, and M_5-shells of Au and Hg, the molar ratio of Hg to Au was estimated to be about 1:6.3. (The cross-section values were obtained by fitting a power law to the data from the evaluated photon data library [41] for photon energies
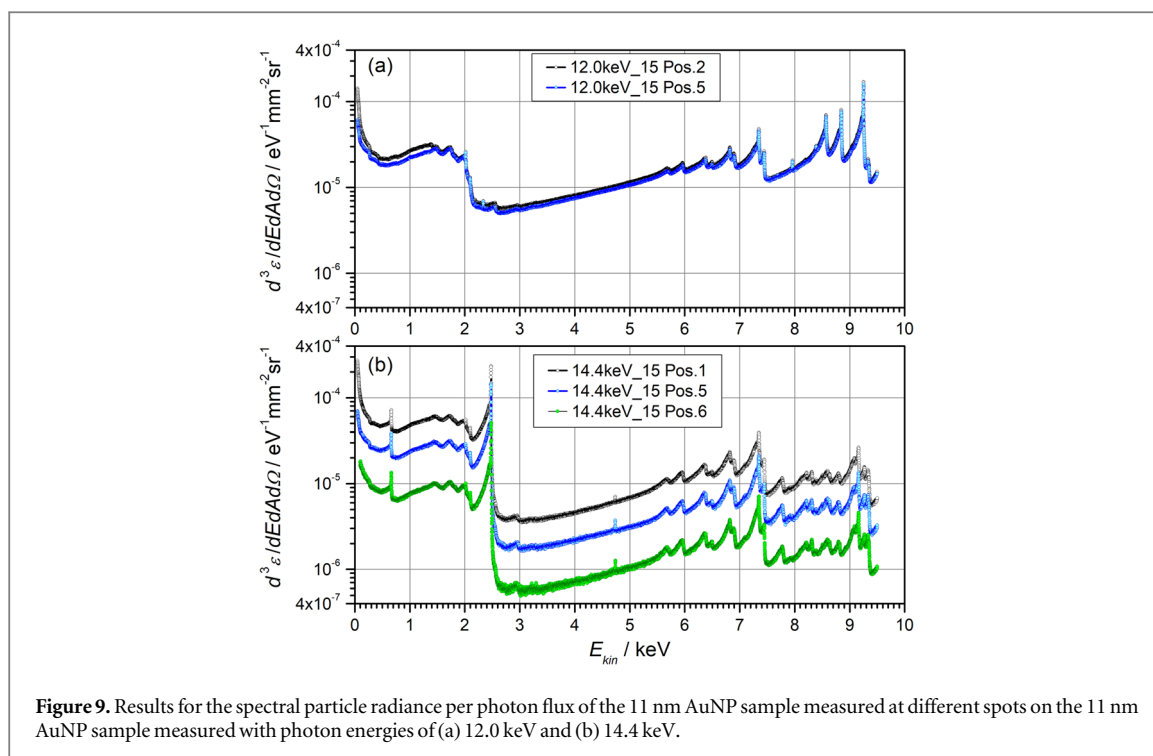
Figure 9. Results for the spectral particle radiance per photon flux of the 11 nm AuNP sample measured at different spots on the 11 nm AuNP sample measured with photon energies of (a) 12.0 keV and (b) 14.4 keV.

Table 2. Energy values of the Auger lines identified in figure 8 compared to the values in the EADL.

Assignment	Experiment E_{peak}/eV	EADL E_{kin}/eV	Prob.	Difference in eV
$L_3M_1M_1$	—	5119.2	0.08 %	—
$L_3M_1M_2$	—	5376.3	0.04 %	—
$L_3M_2M_2$	—	5633.4	0.01 %	—
$L_3M_1M_3$	5684.3	5786.6	2.18 %	−102.3
?	5715.5	—	—	—
$L_3M_2M_3$	5963.6	6043.7	3.66 %	-80.1
$L_3M_1M_4$	6139.8	6219.9	0.26 %	-80.1
$L_3M_1M_5$	6228.0	6308.4	0.42 %	-80.4
$L_3M_2M_4$	6356.2	6477.0	0.18 %	-120.8
$L_3M_3M_3$	6380.1	6454.0	4.68 %	-63.9
$L_3M_2M_5$	6501.9	6565.5	1.55 %	-63.6
$L_3M_3M_4$	6822.2	6887.3	4.90 %	-65.1
$L_3M_3M_5$	6896.0	6975.8	6.72 %	-79.8
$L_3M_4M_4$	7277.7	7320.6	0.68 %	-42.9
?	7317.2	—	—	—
$L_3M_4M_5$	7348.9	7409.1	12.8 %	-60.2
?	7415.5	—	—	—
$L_3M_5M_5$	7449.8	7497.6	8.56 %	-47.8

between 9.0 and 12.5 keV). Thus, when the Hg atoms are inside the nanoparticles, their mole fraction amounts to (13.7 ± 0.5) %. If the Hg atoms are not inside the nanoparticle, but are bound to its surface, about every second surface atom in the AuNP has an Hg atom as a neighbor. (At a diameter of 5.3 nm, about 30% of the gold atoms are located at the AuNP surface).

Figure 6(b) shows the energy spectra of the three samples for 14.4 keV photons in the energy range of the binding energies of the gold L-shells. Again, the dashed lines indicate the binding energies according to the EADL. It can be seen that for both, the gold and mercury lines, the peak positions coincide with the EADL value within ± 1 eV. This is taken as evidence that the electron and photon energy scales are also correct within these limits.
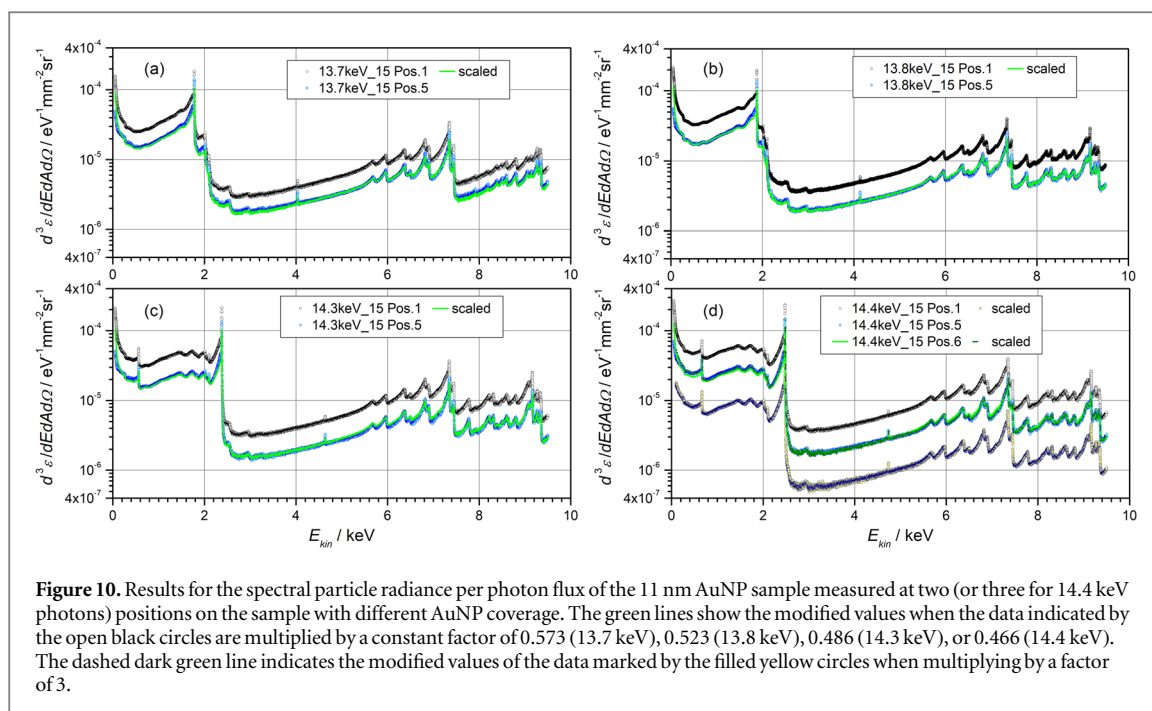
Figure 10. Results for the spectral particle radiance per photon flux of the 11 nm AuNP sample measured at two (or three for 14.4 keV photons) positions on the sample with different AuNP coverage. The green lines show the modified values when the data indicated by the open black circles are multiplied by a constant factor of 0.573 (13.7 keV), 0.523 (13.8 keV), 0.486 (14.3 keV), or 0.466 (14.4 keV). The dashed dark green line indicates the modified values of the data marked by the filled yellow circles when multiplying by a factor of 3.

Figure 7 illustrates the dependence of the Cu-K photoelectron peak in the gold foil measurements on photon energy. The peaks shown in figure 7(a) were fitted with a Lorentz profile to obtain the peak area. The ratio of this peak area to the Cu K-shell photoabsorption cross-section is shown in figure 7(b). The latter was obtained by extracting data for energy points between 10 keV and 15 keV from the database provided with the Penelope code and interpolating based on a power law fit to these data. The relative size of the error bars in figure 7(b) is equal to the relative uncertainty of the peak area resulting from the fit to the data.
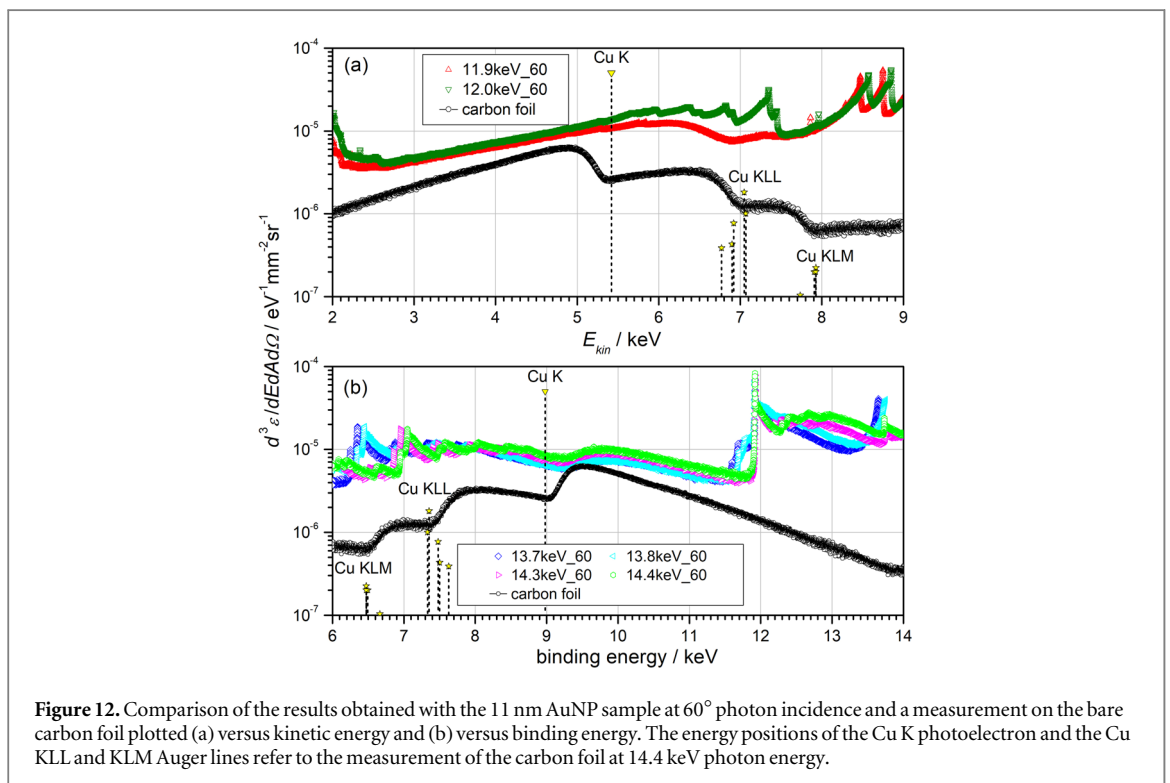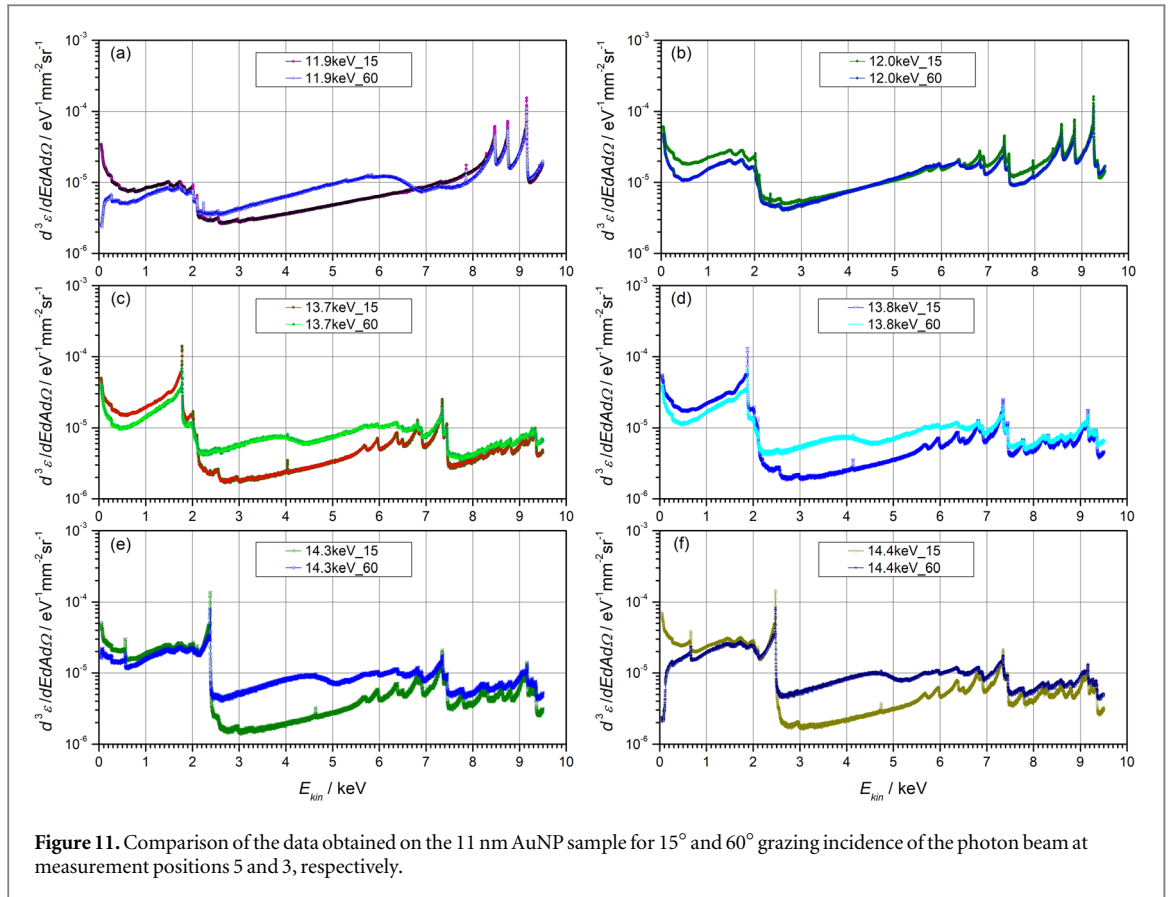
The fact that the ratio of the peak area to the cross-section is essentially constant demonstrates the consistency of the data analysis procedure and that the energy dependence of the photon beam monitor (Supplement 1) and of the electron spectrometer transmission (Supplement 2) have been correctly evaluated.

3.3. Au L Auger electron energies

A completely different situation arises when considering the LMM Auger electrons of gold. The electron spectra measured for the three gold samples after excitation with photons of 11.9 keV and 12.0 keV are shown in figure 8 in the kinetic energy range between 5 keV and 8 keV. This region is the range of gold L_3MM Auger electrons according to the EADL [39]. The respective electron emission peaks are expected for the 12.0 keV photon energy, whereas the L_3-edge of gold cannot be excited by 11.9 keV photons. The small features seen in the lowest curve of the 11.9 keV measurement on the 5.3 nm AuNP samples suggest that the incident photon beam may contain a small fraction of higher-energy photons from the higher orders of the monochromator and undulator. In contrast to the data from the 11 nm AuNPs and the gold foil, the 11.9 keV measurements of this sample do not show the monotonous increase with electron energy. This is due to a background of electrons produced in the sample holder that will be discussed in more detail in the next sections.
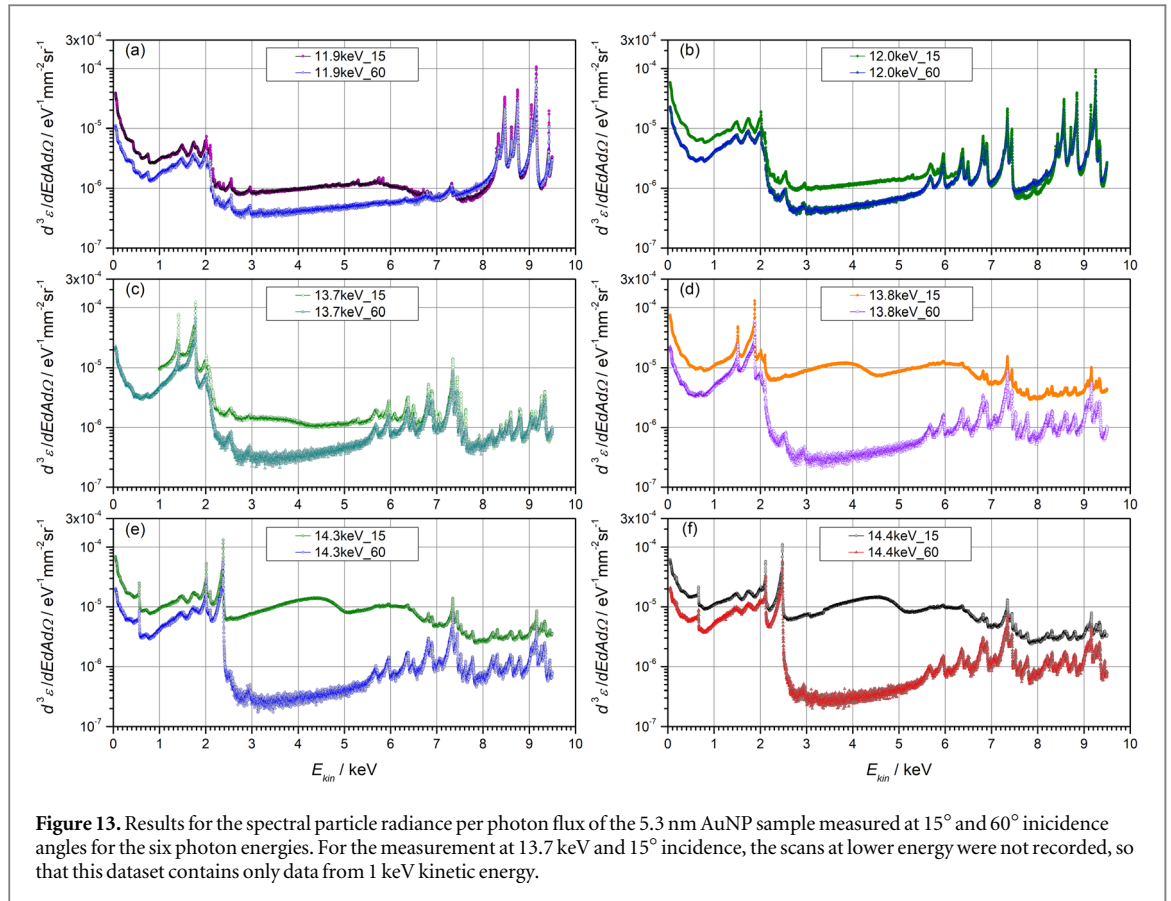
The peaks were assigned in figure 8 based on ascending energy and the peak intensities given in the EADL [39]. It is worth noting that the peaks appear at the same energies for all samples, although for the larger AuNPs and the Au foil, the low-energy tailing is very pronounced. This suggests that any effects of the local environment of the absorbing atoms in the nanoparticles are already fully active for the 5.3 nm AuNPs. It should be noted that these nanoparticles contain about 4000 atoms.

The energies of the peak maxima are listed in table 2 together with the corresponding values taken from the EADL [39]. Significant discrepancies are observed for all peak energies, in some cases exceeding 100 eV. These shifts to lower energies are expected since the Auger energies reported in the EADL are calculated from differences of the binding energies of the electron levels involved. It is not taken into account that the de-excitation occurs for a positive ion and that there may be a rearrangement of the orbitals and their binding energies before the non-radiative transition occurs. This warrants a separate investigation, which will be presented in the third part of the paper, where the experimental data are used to benchmark the 'radial' code [34].

Figure 11. Comparison of the data obtained on the 11 nm AuNP sample for 15° and 60° grazing incidence of the photon beam at measurement positions 5 and 3, respectively.

Figure 12. Comparison of the results obtained with the 11 nm AuNP sample at 60° photon incidence and a measurement on the bare carbon foil plotted (a) versus kinetic energy and (b) versus binding energy. The energy positions of the Cu K photoelectron and the Cu KLL and KLM Auger lines refer to the measurement of the carbon foil at 14.4 keV photon energy.

3.4. Electron energy spectra of the 11 nm AuNP sample

Measurements were performed on the 11 nm AuNP samples at 15° and 60° grazing incidence of the photons. The rationale was that the two different irradiation geometries would allow discriminating effects of multilayers (which are more pronounced for 60° grazing incidence) and monolayers (at 15°), as well as the effect of impurities, which have been reported in other work [42–46]. In the absence of multilayers and impurities, the

Figure 13. Results for the spectral particle radiance per photon flux of the 5.3 nm AuNP sample measured at 15° and 60° inicidence angles for the six photon energies. For the measurement at 13.7 keV and 15° incidence, the scans at lower energy were not recorded, so that this dataset contains only data from 1 keV kinetic energy.

energy emission spectra for the two incidence angles should match if the nanoparticle surface density is the same in both measurements.

It was found during the beamtime (cf figure S4.1) and confirmed by the STEM measurements performed afterwards [36] that the surface is non-uniformly covered with AuNPs. Therefore, different measurement runs probing different regions of the sample resulted in different values of particle radiance. This is illustrated in figure 9, where results from measurements at two energies and 15° grazing incidence of the photon beam are plotted.

Figure 9(a) shows a comparison of two measurements at 12 keV photon energy performed on almost the same surface area of the sample. In this case, there is good agreement of the two spectra with some notable deviations at smaller electron energies. This is explained by the fact that in the first experiment the energy scan over the second energy range (100 eV − 1.2 keV) initially failed and was only repeated after a longer interval (about 6 h) at a slightly different spatial position on the sample.

Figure 9(b) shows three measurements at 14.4 keV photon energy in different locations on the sample. Measurement position 1 was a spot that gave a maximum signal and was probed first to obtain a good signal-to-noise ratio (cf figure S4.1(a) and (b) in Supplement 4). The posterior STEM investigations of the sample indicated the occurrence of so-called 'coffee rings' on the sample where the AuNPs occur as multilayers [36]. Therefore, position 1 is attributed to a region on the sample surface with multilayer coverage. Position 5 was also located in the outer parts of the sample (figures S4.1(c) and (d)) but is expected to be an area where monolayer coverage prevails. Position 6 was located in the central region of the sample (figure S4.1(e) and (f)) where the AuNPs occur in (sub-)monolayers [36].

As can be seen in figure 9(b), the spectra at different coverages appear to have the same relative energy dependence with an almost constant offset on the logarithmic scale, meaning there is a constant factor between them.

This is further illustrated by figure 10, which shows a comparison of measurements at 15° photon beam incidence made for the two positions on the sample with the four higher photon energies. The data shown in figure 10 corroborate that the measurement results for the two sample positions are offset by a constant factor. This is demonstrated by the green lines in figure 10. Here, the data represented by black symbols have been multiplied by a constant factor (as given in the figure caption) which bring them into agreement with the blue symbols (data measured at position 2). The same good agreement is found when the data measured at position 6

(yellow filled circles) are multiplied by a factor of three, giving the dark green dashed curve. This suggests that the shape of the emitted electron spectra is mainly determined by the nanoparticles themselves.

Figure 11 shows a comparison of the spectra obtained on the 11 nm AuNP sample for measurement position 5 at 15° grazing incidence and for measurement position 3 at 60° incidence (in the plateau region of surface coverage [36], cf figure S4.4) for all photon energies. The data measured at 12.0 keV for the two incidence angles appear to be offset by a constant factor (figure 11(b)), reflecting the different AuNP coverage at the respective measurement positions. For all other photon energies, large discrepancies in the relative spectral-shape are evident in the electron energy range between 2.5 keV and 7 keV.

The origin of these discrepancies is a so-called Tougaard background [47, 48] of electrons produced in the copper sample holder. This is supported by figure 12(a), which shows a comparison of the results on the 11 nm AuNP sample for 11.9 keV and 12.0 keV photons at 60° incidence with the single measurement on the bare carbon foil made at 14.4 keV and 15° incidence. The features appearing in the carbon foil data between 5.3 keV and 8 keV are also visible for the 11.9 keV data on the AuNP sample with similar relative shape. Their upper energies agree with the energy range of the Cu KLM and Cu KLL Auger electrons.

Figure 12(b) shows the data for the other photon energies with the same carbon foil spectrum plotted against binding energy. It is evident that the feature observed between 9 keV and 11.5 keV binding energies are matched for the different photon energies, suggesting a photoelectron line as their origin. Their onset is at slightly higher energies than the Cu-K binding energy from the EADL.

3.5. Electron spectra of the 5.3 nm AuNP sample

For the sample with 5.3 nm AuNPs, only one measurement run was performed per incidence angle of the photon beam. The respective results are shown in figure 13, where large discrepancies between the measurements at the two incidence angles can also be seen. In contrast to the results obtained for the 11 nm AuNP samples, for this sample the Tougaard background is seen in the 15° experiments, while it does not appear to be present in the 60° measurements.

This finding is supported by the observation in figure S4.6 that the signal ratio of 15° to 60° at the chosen measurement position is about 6 for the energy of the Au L3 photoelectron line (figures S4.6(a) and (c)), while it amounts to more than 10 for the Au $L_3M_5M_5$ Auger line (figures S4.6(b) and (d)).

4. Discussion

4.1. Tougaard background

The appearance of the Tougaard background in the experiments with the 11 nm AuNP sample is related to the fact that a 50 nm carbon foil covered with a (sub-)monolayer of AuNPs absorbs less than 0.6% of the photons at a 15° angle of incidence and less than 0.2% at 60°. At an incidence angle of 15°, the photon beam is expected to hit the sample holder on the aluminum support with a lateral offset (as seen from the spectrometer) of about 2.5 mm at a location shielded by the front edge (figure 14(a)). At an angle of incidence of 60°, on the other hand, the photon beam impinges on the copper block of the sample holder at a point about 1.2 mm from the spectrometer axis (figure 14(b)).

For the 5.3 nm AuNP sample, the Tougaard background is observed in the 15° measurements, but not at 60° incidence. One possible explanation for this unexpected observation is that in the 60° measurements on this sample, the photon beam hits a spot on the carbon foil that is on top of the aluminum support, so that the photon beam reaches the copper sample holder at a location below the aluminum layer (figure 15(b)).

In the 15° measurements, it is likely that the beam passed close to the edge of the aluminum support and hit the Cu sample holder below the self-supporting part of the carbon substrate (figure 15(a)). Since the carbon substrate has a curvature where it covers the aperture in the aluminum support (figure 4), the angle of incidence is reduced when the photon beam hits the sample near the circumference of the hole in the aluminum support. This implies that the irradiated surface area is enhanced by a factor which is greater than 1/sin(15°). This would explain why the 15° data are significantly larger than the 60° data for the three higher photon energies in the electron energy range above 8 keV, where electrons originating in the Cu sample holder cannot contribute to the measured signal. The magnitude of the discrepancies varying with photon energy can be attributed to slight shifts in beam position on the sample as the photon energy changes.

When the incident photon beam is dumped in the sample holder, the relaxation of core-ionized Cu or Al atoms can also produce fluorescence photons. Some of these photons interact with the AuNPs or the supporting carbon foil and generate electrons that contribute to the measured signal. The signal contribution originating from the Cu and Al fluorescence photons was estimated from the linear photon attenuation coefficients of the four materials (Au, carbon, Cu, Al) from the XCOM database [49]. The fluorescence photon energies and
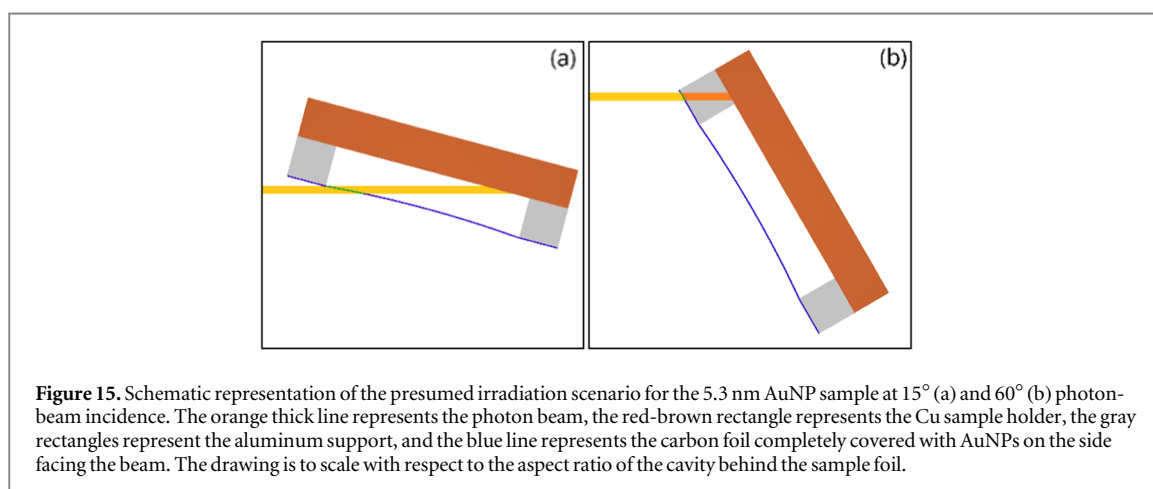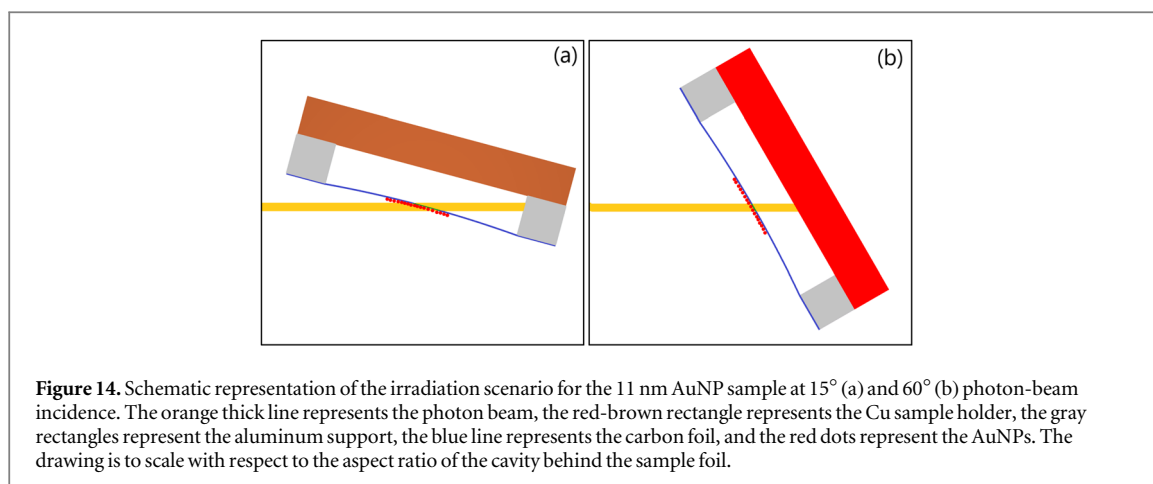
Figure 14. Schematic representation of the irradiation scenario for the 11 nm AuNP sample at 15° (a) and 60° (b) photon-beam incidence. The orange thick line represents the photon beam, the red-brown rectangle represents the Cu sample holder, the gray rectangles represent the aluminum support, the blue line represents the carbon foil, and the red dots represent the AuNPs. The drawing is to scale with respect to the aspect ratio of the cavity behind the sample foil.

Figure 15. Schematic representation of the presumed irradiation scenario for the 5.3 nm AuNP sample at 15° (a) and 60° (b) photon-beam incidence. The orange thick line represents the photon beam, the red-brown rectangle represents the Cu sample holder, the gray rectangles represent the aluminum support, and the blue line represents the carbon foil completely covered with AuNPs on the side facing the beam. The drawing is to scale with respect to the aspect ratio of the cavity behind the sample foil.

Table 3. Uncertainty budget of the spectral particle radiance per photon flux for the three samples studied.

Source of uncertainty	Scope	11 nm AuNP		5.3 nm AuNP		Au foil
		15°	60°	15°	60°	15°
Electron spectrometer transmission	global	33 %	33 %	33 %	33 %	33 %
Electron counting	data point	2 %–15 %	3 %–27 %	3 %–12 %	7 %–30 %	2 %–5 %
Energy range merging	spectrum	0.8 %–2.9 %	1.1 %–22 %	0.7 %–4.6 %	1.5 %–12 %	0.9 %–2.2 %
Energy scale	data point	2 %–10 %	2 %–10 %	2 %–10 %	2 %–10 %	2 %–10 %
Photon monitor measurement	data point	0.6 %	0.6 %	0.6 %	0.6 %	0.6 %
Photon monitor calibration	spectrum	2.5 %–4.4 %	2.5 %–4.4 %	2.5 %–4.4 %	2.5 %–4.4 %	2.5 %–4.4 %
Sample inhomogeneity	sample	5 %	5 %	10 %	10 %	0.5 %
Angle of incidence	sample	5 %	2 %	5 %–50 %	2 %	5 %
Photon beam area	global	20 %	20 %	20 %	20 %	20 %
Total uncertainty		39 %–43 %	39 %–53 %	40 %–66 %	41 %–53 %	39 %–41 %

transition probabilities were obtained from the EADL database [39, 40]. The photon interaction cross sections for the Au M-shells were taken from the database provided with the Penelope code [50].

Cu K_α photons occur with a probability of about 39% and have energies slightly above 8 keV. Cu K_β photons have energies slightly below 9 keV and occur with a probability of about 5%. The energy of Al K_α photons is slightly below 1.5 keV, their production probability amounts to about 4%.

For the case of irradiation shown in figure 14(a), the estimated ratio of the flux of Cu K_α and K_β fluorescence photons to the flux of photons from the beamline was about 3.5×10^{-4} and 4.5×10^{-5}. This estimate is based on the assumption that the fluorescence photons can produce detectable electrons over the whole area covered with AuNPs (about 1 mm^2). The self-absorption of the fluorescence photons in the Cu material was taken into account, while the attenuation in Al was neglected.

This additional photon flux leads to the production of Au M-shell photoelectrons with energies between 4.6 keV and 5.8 keV for Cu K_α and between 5.6 keV and 6.8 keV for Cu K_β photons. The estimated ratio between the peak intensity of these photoelectrons and of those produced by the incident photons is about 0.1% for the Au M_1 line and between 0.15% and 0.25% for the Au M_5 line (at 11.9 keV and 14.4 keV photon energy, respectively). These values are negligibly small and explain why the corresponding peaks are not seen in figure 6.

In the geometry shown in figure 14(b), the solid angle subtended by the AuNP-covered surface is much larger (as seen from the region where the fluorescence photons are generated). In this case, the estimated flux ratio of Cu K_α and K_β to the incident photons is about 1.3×10^{-2} and 1.7×10^{-3}. The estimated ratio of Au M-shell photoelectrons produced by Cu fluorescence photons to those of the 11.9 keV beam ranges from 3.4% for the Au M_1 line to 5.8% for the Au M_5 line. At 14.4 keV photon energy, the corresponding ratio is 9.4% for the Au M_5 line. Closer inspection of figure 11(a) shows that the Au M_3, M_4, and M_5 lines generated by Cu K_α photons can indeed be seen in this case.

A similar estimate was made for the signal from the carbon foil. Assuming that the relevant area was a factor of 10 larger than for the AuNP-covered surface, the ratio of photoelectrons produced in the carbon foil by fluorescence photons to those from the incident beam was about 2% for an incidence angle of 15° and between 52% and 82% for the 60° geometry. However, the ratio of photoabsorption interactions in the carbon substrate to those in the AuNP sample is only about 2%. Therefore, the increase in background signal from electrons generated in the carbon foil by Cu fluorescence is negligible.

For the additional contribution of Al K_α photons, an upper limit was estimated for the irradiation geometry shown in figure 14(a) by assuming that the photon beam is completely absorbed in aluminum. The resulting ratio of fluorescence photons to the incident beam was about 1.0×10^{-5}. The ratio of fluorescence photon-generated photoelectrons from the N, O, and P-shells of gold to incident photons was estimated to be 0.16%. The cross sections for photoabsorption on the outer shells of gold vary between 10% and 5% of the total photoabsorption cross section for photon energies between 11.9 keV and 14.4 keV. This means that the measured electron spectrum between 720 eV (energy of an Au N_1 photoelectron excited by Al K_α) and 1480 eV may contain a contribution of photoelectrons from outer Au shells that are produced by Al fluorescence. This is especially true in the case of irradiation geometry as shown in figure 15(b).

Proper modeling of the Tougaard background of electrons produced in the Cu and Al parts of the sample holder (and of the signal contributions from the Cu and Al fluorescence photons) is one of the challenges in the ongoing quantitative analysis of the spectra [51]. This will be presented in part 4 of the paper. The remainder of this discussion will focus instead on the plausibility of the results in terms of absolute magnitude, their associated measurement uncertainty, and their caveats.

4.2. Uncertainty budget

Table 3 shows an indicative uncertainty budget for the particle radiance measurement results considering only the dominant uncertainty contributions. The various sources of uncertainty are listed in the first column, and the scope of the respective uncertainty is stated in the second column. The term 'scope' is used here in the sense that the uncertainty contribution applies to all data points within the respective scope, so that these contributions are fully correlated for these data points. Examples include the photon beam area and the spectrometer transmission for the reference energy and reference retarding ratio. This reference transmission value (cf Supplement 3) is the same for all data points of all datasets and photon energies.

In contrast, the electron counting statistics are specific to each data point. As can be seen from the second row in table 3, the respective values range between 2% and 30%. Larger uncertainties occur for the 60° measurements due to the smaller sample area (and, hence, the smaller number of AuNPs) irradiated by the photon beam.

The uncertainty component for electron range merging of the spectra of different electron ranges is essentially the standard uncertainty of the ratio of transmission values for different retarding ratios determined from the measurements in overlapping energy intervals. The large range of uncertainties for the 60° measurements on the 11 nm sample are due to the two measurements at 14.4 keV, where there was a strong drift in the photon monitor signal. Omitting these two values reduces the upper limit of this uncertainty contribution to 4.2%

The uncertainty contribution from variations of the energy scale of photons or electrons was estimated from the deviations from a constant value. Such deviations were seen in the ratios between different spectra measured for the same photon energy for the 11 nm AuNP sample (figures S4.3 and S4.5). These values were also used for the other samples.

The uncertainty of the photon monitor measurements was derived from a systematic review of the monitor current measurements in all experiments. The uncertainty of the photon monitor calibration depends on the

Table 4. Probability per incident photon of the two types of AuNPs to experience a photon interaction and its product with the average surface area density c_s of AuNPs for a hexagonal close-packed monolayer.

Photon energy (keV)	5.3 nm AuNP		11 nm AuNP	
	p_i	$n_i\,(\mathrm{mm}^{-2})$	p_i	$n_i\,(\mathrm{mm}^{-2})$
11.9	1.17×10^{-12}	0.016	8.63×10^{-12}	0.048
12.0	2.81×10^{-12}	0.038	2.08×10^{-11}	0.116
13.8	1.97×10^{-12}	0.026	1.46×10^{-11}	0.081
13.9	2.67×10^{-12}	0.036	1.98×10^{-11}	0.110
14.3	2.45×10^{-12}	0.033	1.82×10^{-11}	0.101
14.4	2.78×10^{-12}	0.037	2.06×10^{-11}	0.115

Table 5. Integral of the electron yield per photon interaction over the measured electron energy range multiplied by 4π Sr for the particle radiance obtained for the different photon energies at the different measurement positions on the two AuNP samples. The values have been calculated assuming a hexagonal close-packed monolayer of AuNPs.

Photon energy (keV)	Measurement position on 11 nm AuNP sample						5.3 nm AuNP sample	
	1	2	3 (60°)	4	5	6	15°	60°
11.9	—	—	24.6	18.4	23.1	—	6.4	4.0
12.0	—	19.2	15.1	—	17.4	—	4.3	2.7
13.7	20.1	—	14.2	—	12.1	—	4.6	3.4
13.8	19.4	—	11.5	—	10.2	—	10.7	2.7
14.3	20.5	—	12.1	—	10.1	—	11.3	2.8
14.4	22.0	—	11.4	—	10.6	3.5	10.2	2.9

photon energy (Table S1.1), and this uncertainty contribution is therefore correlated for all measurements at the same photon energy.

The uncertainty contribution due to sample non-uniformity was estimated from the position scans on the AuNP samples shown in figures S4.1, S4.4, and S4.6 for an estimated change in photon beam position of $\pm\,50$ μm. For the gold foil, this uncertainty contribution was assumed to be an order of magnitude smaller than for the 11 nm AuNP sample, which still seems conservative.

For the 11 nm AuNP sample and the Au foil, the uncertainty contribution of the angle of incidence was estimated for the case where the true angle of incidence is within $\pm3°$ of the nominal value with a uniformly distributed probability. For the 5.3 nm AuNP sample, the values for the 60° measurements were estimated to be the same as for the other sample. And for the 15° measurements, the uncertainty was estimated to be up to 2.5 times higher (for the three higher photon energies), due to the assumed location of the irradiated area near the circumference of the hole in the aluminum support (figure 15(a)).

The row in table 3 referring to the photon beam area only gives the uncertainty of the area determination (Supplement 2). The size of the photon beam is determined solely by the imaging optics and the size of the electron beam in the storage ring within the undulator and, therefore, the same for all photon energies.

As can be seen from the last row of table 3, the total uncertainty is about 40% for the 15° measurements on the 11 nm AuNP and the Au foil samples. Furthermore, the total uncertainty is up to more than 50% for the 60° measurements on the two AuNP samples, and up to more than 60% for some of the 15° measurements on the 5.3 nm AuNP samples. In the first case with the lowest total uncertainty, the two dominant uncertainty contributions come from the spectrometer transmission and the photon beam area. In the 60° measurements, the smaller signal gives rise to a large contribution from electron counting statistics which turns into the second most important uncertainty for some data points of these measurements.

4.3. Plausibility checks

The effective particle radiance is a quantity that characterizes the overall electron emission from the sample, including the emitted Auger and Coster-Kronig electrons as well as secondary electrons produced by inelastic electron interactions in the sample. It is the superposition of the particle radiance from the actual sample, $d^3\varepsilon_s/dAdEd\Omega$, and the background contribution, $d^3\varepsilon_b/dAdEd\Omega$.

Table 6. Ratio of the integral of the electron yield per photon interaction multiplied by the electron energy to the photon energy for the particle radiance obtained for the different photon energies at the different measurement positions on the two AuNP samples.

Photon energy (keV)	Measurement position on 11 nm AuNP sample						5.3 nm AuNP sample	
	1	2	3	4	5	6	15°	60°
11.9	—	—	12.39	8.82	11.56	—	2.36	1.76
12.0	—	7.97	6.77	—	7.43	—	1.31	1.02
13.7	4.79	—	4.20	—	2.89	—	1.01	0.65
13.8	4.73	—	3.43	—	2.50	—	2.84	0.54
14.3	4.55	—	3.38	—	2.21	—	2.87	0.54
14.4	4.66	—	3.14	—	2.20	0.73	2.53	0.54

$$\frac{d^3\varepsilon}{dA\ dE\ d\Omega} = \frac{d^3\varepsilon_s}{dA\ dE\ d\Omega} + \frac{d^3\varepsilon_b}{dA\ dE\ d\Omega} \tag{3}$$

For the AuNP samples, a more relevant quantity is the yield of emitted electrons per photon interaction in a nanoparticle, $d^2y_{np}/dEd\Omega$. This quantity is doubly differential in energy and solid angle and is given by

$$\frac{d^2y_{np}}{dE\ d\Omega}(E_e) = \frac{1}{n_i(E_p)}\frac{d^3\varepsilon_s}{dA\ dE\ d\Omega} \tag{4}$$

where n_i is the mean area number density of AuNPs undergoing a photon interaction. n_i is given by

$$n_i(E_p) = p_i(E_p) \times c_s \tag{5}$$

where p_i is the probability of an incident photon of energy E_p to interact with an AuNP, and c_s is the number of AuNPs per surface area (surface number density).

The probability p_i can be estimated from the known particle size, beam size, and literature data of the photon interaction cross sections as follows

$$p_i(E_p) = \frac{\mu_{tot}(E_p)\ V_{np}}{A_b} \tag{6}$$

where μ_{tot} is the total linear attenuation coefficient, V_{np} is the volume of the AuNP, and A_b is the beam cross-sectional area.

In the evaluation of equation (6), the average volume was used. This was calculated assuming a Gaussian distribution of the AuNP diameters. A standard deviation of 0.9 nm was used for the 11 nm AuNPs. (The value of 1.8 nm given in [36] corresponded to two standard deviations). For the 5.3 nm AuNPs, it was assumed that the relative standard deviation of the diameter distribution was the same as for the two types of smaller AuNPs reported in [52]. This resulted in a standard deviation of 1.5 nm for the AuNP diameter.

The linear attenuation coefficients were obtained by adding the requested energies in the online search form of the XCOM database [49]. The resulting values of p_i for the two nanoparticle types are listed in the second and fourth columns of table 4.

The values of the product $n_i = p_i \times c_s$ are shown in the third and the last columns of table 4 for the surface density of a hexagonal close-packed (HCP) monolayer of mean-diameter AuNPs with a 2 nm thick PEG or PEG-MUA coating. The respective values are $c_s = 5.13 \times 10^9$ mm^{-2} for the 11 nm AuNPs and $c_s = 1.34 \times 10^{10}$ mm^{-2} for the 5.3 nm AuNPs.

When the doubly differential yield of emitted electrons per photon interaction in a nanoparticle was known for all emission angles and the complete energy range, the total number of electrons emitted per photon interaction in the AuNP could be calculated by integrating over energy and the whole solid angle. Calculating the integral after multiplying the yield by the electron energy would give the average energy per photon interaction that is transported out of the nanoparticle by electrons generated in it. These electrons are produced by photoelectric absorption, by atomic relaxation after photoabsorption, and by interactions of the electrons emitted from the absorbing atom in the AuNP.

The calculation of these quantities from the experimental data is hampered by the fact that the background particle radiance $d^3\varepsilon_b/dA\ dE\ d\Omega$ and the angular distribution of the emitted electrons are not known *a priori*. Moreover, due to the limited energy range of the HAXPES spectrometer, only a part of the electron energy spectrum could be detected in the experiments.

Nevertheless, estimates can be made by replacing $d^3\varepsilon_s/dAdEd\Omega$ in equation (4) with $d^3\varepsilon/dA\ dE\ d\Omega$ and using the values of n_i for a monolayer coverage (table 4). Integrating this estimate for $d^2y_{np}/dE\ d\Omega$ over the

measured energy range and multiplying it by 4π (i.e., assuming isotropic emission) gives the values listed in table 5.

Several observations can be made about table 5. One is that the values obtained in measurement positions 1, 2, and 4 are approximately the same for all photon energies. That positions 2 and 4 give the same value as position 1 is surprising, since they were located regions of lower surface coverage (figure S4.1(d)). However, this paradox could be due to a coincidence, since for positions 3 and 5, the values at the lower photon energies are significantly increased compared to the higher photon energies.

The values obtained at position 5 for the four higher photon energies are about half those for position 1, which is expected from what is shown in figure 10. Similarly, the factor of 3 between the values for 14.4 keV at positions 5 and 6 are also expected from the results shown in figure 10(d). It is worth noting that for both position 3 and position 5, there is a decreasing trend for the three lower photon energies and essentially constant values for the three higher photon energies.

The fact that for 14.4 keV, the value at position 3 is about 20% higher than the value at position 5—even though both positions are in the plateau region—is explained by the extra electrons from the Tougaard background present in the measurements at position 3.

For the 5.3 nm AuNP sample, the values for 60° are more or less independent of photon energy, whereas clear differences between photon energies are found for the 15° measurements.

The data shown in table 5 are the estimated number of electrons with energy less than 9.5 keV emitted per AuNP undergoing photon interaction. They mainly reflect the differences between measurement positions and incidence angles already seen in the figures. Therefore, a more relevant key figure is obtained by integrating the product of the estimated $d^2 y_{np}/dE\ d\Omega$ and the electron energy over the measured energy range, multiplying the result by 4π and dividing by the photon energy. This quantity is an estimate of the proportion of the energy transferred by the photon interaction that is transported out of the AuNP by electrons with kinetic energies below 9.5 kV. This quantity is listed in table 6.

While the same observations as in table 5 can be made about trends with photon energy and ratios between different columns, the values now allow quantitative interpretation. For an isolated AuNP, this quantity must be significantly smaller than unity. This is because the integral is performed over only a part of the electron energy spectrum and the total energy transported out of the AuNP cannot exceed the photon energy. Ad hoc simulations with the Penelope code [50, 53] forcing photon interaction in the AuNPs indicated that about 70% of the photon energy was found in the energy spectrum of escaping electrons with energies below 9.5 keV.

For AuNPs in a monolayer on a thin carbon substrate, the number of electrons emitted from the sample in the direction of the electron spectrometer is enhanced by the scattering of emitted electrons on neighboring AuNPs. For an HCP monolayer of 5.3 nm AuNPs with a 2 nm PEG coating, the solid angle covered by the first and second nearest neighbors is about 2 sr or 16% of 4π. In addition, for the 11 nm AuNPs, the respective value is 27% of the full solid angle. However, these nanoparticles contain eight times more gold atoms than the smaller AuNPs, resulting in correspondingly stronger electron scattering. Moreover, STEM investigations of the 11 nm AuNP sample showed a significant occurrence of multilayers [36], where the coordination number of the nearest neighbors can be a factor of 2 higher than for an HCP monolayer.

Thus, ignoring the data affected by the Tougaard background, the numbers in table 6 indicate that for the 11 nm AuNPs, electron scattering on neighboring AuNPs results in a significant enhancement of the number of electrons measured with the spectrometer. Moreover, the relative magnitude of this enhancement depends on the surface coverage and the presence of multilayers.

For the measurements at position 3 and 5 of the 11 nm AuNP sample and for 60° incidence on the 5.3 nm AuNP sample, the trend of increasing values with decreasing photon energy is more pronounced in table 6 than in table 5. The weighting by electron energy applied in deriving the data in table 6 implies that these values are predominantly due to the M-shell photoelectron peaks in the measurements at 11.9 keV and 12.0 keV photon energy.

In contrast to Auger electrons, the emission direction of photoelectrons has a non-isotropic distribution peaking along the direction of the electric field vector of a linearly polarized photon beam. The respective anisotropy can be described in terms of Legendre polynomials [54, 55]. For excitation from an s-orbital of an isolated atom, the number of electrons ejected along the direction of the electric field vector is higher than for isotropic emission by a factor of 3. However, the M_3, M_4, and M_5 lines originate on p-orbitals for which this enhancement is smaller.

Therefore, the anisotropy of photoelectron emission cannot fully explain the pronounced increase of the values listed in table 5 and table 6 with decreasing photon energy. It should also be noted that the peculiarities in the variation of the photon monitor calibration factor and photon flux (Table S1.1) do not provide an explanation either. Due to the energy dependence of the photon interaction coefficients, higher values of the

calibration factor are expected at lower photon energies. However, higher calibration factors would lead to even larger values of the figures of merit at the two lowest photon energies.

The larger contribution of M-shell photoelectrons in the spectra at the lowest photon energies could also provide another possible explanation. These electrons have energies in the range between 5 keV and 9.5 keV, giving them a range of a few hundred nm in gold. Neighbors within this range could therefore contribute to the measured signal by electron scattering. What argues against this explanation is that the ratios of the values at position 1 (and position 6) to those at position 5 of the 11 nm AuNP sample are approximately the same in both table 5 and table 6.

The most likely reasons for the increased values at the lower two photon energies are as follows: First, that the position of the photon beam on the sample varies with photon energy, with the beam with lower photon energies hitting a spot with higher AuNP coverage. Second, that there is probably a Tougaard background from Al K photoelectrons. It can be seen from figure 12(a) that this background contributes most strongly for Cu in the energy range between 100 eV and 2 keV below the K-shell photoelectron energy. Assuming a similar relationship for the Al photoelectrons and considering that the K-shell binding energy of Al is about 1.56 keV, this background would affect the signal in the energy range of above 8 keV. This applies to the electron spectra measured at 11.9 keV and 12.0 keV photon energy, but not at higher photon energies.

In terms of absolute numbers, the values in the last column of table 6 suggest that the 5.3 nm AuNPs do not form an HCP monolayer and/or have a coating thickness larger than the assumed 2 nm. For the 11 nm AuNP sample, position 6 would be a region of HCP monolayer coverage, and position 5 would already have multilayers. This is in contradiction to the estimated average AuNP coverage in the order of 0.2 monolayers reported in [36]. It must be noted, however, that this estimate of coverage was based on the nominal concentration of the AuNP solution and is not a result from the STEM measurements. Furthermore, the area covered by the AuNPs that was estimated based on the linear dimensions read from figure S4.4 is only about 2/3 of the value determined from the STEM images in [36], which suggests that the average coverage was higher by about 50% for the sample used in this study.

An approximate quantitative analysis of the STEM images suggests that some of the AuNPs have the shape of prolate ellipsoids standing with the long axis (elevated by about 20% relative to the short axis) pointing upward. In addition, the preliminary characterization of the AuNP solution by small angle x-ray scattering (SAXS) indicates a significant fraction of about 30% of AuNP dimers and trimers and an increased average volume of the AuNPs by about 25% compared to the STEM values. All these factors suggest the actual probability for photon interaction could be increased by a factor of about 1.6. Even after correcting the values for the 11 nm AuNP sample in table 6 with this increased photon interaction probability, the conclusion still remains, that only the measurement at position 6 was for (sub-)monolayer coverage. All other measurement spots were, however, in regions with significant multilayer coverage.

4.4. Influence of surface contamination

The experiments were conducted on the samples without any further surface cleaning procedures after transferring them to the vacuum system of the experimental station. The reason for this was that previous studies had shown that treating the samples with ion beam sputtering can lead to the destruction of the AuNP coating or the removal of the AuNPs from the sample surface [37]. The setup did not allow the use of the discharge etching method described in [46] either. Therefore, it must be assumed that the samples are covered with surface impurities due to the adsorption of residual gas atoms as well as residues of the chemicals used in their preparation, as already seen in figure 6. The XPS investigations on similar 11 nm AuNP samples showed surface coverage with hydrocarbons and other carbon-based molecules [37].

As Henneken *et al* have shown, surface contamination can drastically reduce the electron emission properties of metal surfaces under soft x-ray irradiation [42–44]. Hespeels *et al* also found a strong suppression of low-energy electron emission from AuNP samples due to carbon surface contamination [46]. Evidence for this can also be seen in the 60° data in figure 11(a).

Therefore, the measured electron radiance at low kinetic energies may be underestimated due to surface contamination. This could be another reason why the two sets of measured data at position 3 of the 11 nm AuNP sample show poor reproducibility in the energy range up to a few hundred eV (cf figures S4.3 and S4.5). In fact, figures S4.3(c) to (f) suggest that surface contamination is more prevalent in the regions with monolayer coverage. This is not confirmed by figure S4.5, which shows a higher average signal associated with a reduction at low energies. This indicates that not only the surface density of AuNPs, but also the density of the surface contamination is strongly non-uniform. However, it is important to note that this contamination significantly affects the measured particle radiance only at lower electron energies, as was also found in [46]. Conversely, this means that the results at higher energies can very well serve as benchmark data for simulations.

4.5. Use of the results for benchmarking

In the first report by Li *et al* [18] on the results of the code comparison, discrepancies between electron spectra reported by different participants were in some cases above one order of magnitude. The literature review by Moradi *et al* [16] also included examples of order-of-magnitude differences between the results of various MC simulation studies of nanoparticle radiation effects.

Given this situation, the fact that the experimental dataset produced in this study is only for six photon energies and is subject to large uncertainties does not seem to impair its use as a benchmark. This is simply because the spread of results in the literature is much larger. Therefore, tables of the results are provided as Supplements 5 to 10 to this article.

During the re-evaluation of the results from the multicenter comparison, which led to the publication of a corrigendum [19], it was discovered that two participants had used the cumulative distribution of the x-ray spectra as the photon spectrum instead of the probability distribution. At the same time, these participants also used a different photon beam size. The synergy of effects resulting from the two deviations from the exercise definition made it very difficult to identify the origin of the deviations of the results of these two participants from the others. Reference simulations for a fixed photon energy would have made it easier to identify the geometry problem.

The measured data refer to two specific nanoparticle sizes with particular coatings and layer thicknesses. Therefore, when using the data for benchmarking simulations in studies interested in different sizes of nanoparticles and/or coating thicknesses, two simulations are required: one for the sizes used here and one for the sizes to be studied. Once set up, changing dimension and/or material compositions in a simulation geometry is not too much of an effort and should be less error-prone.

Within certain limits, the measured data can also be used directly for other nanoparticle sizes and coating thicknesses. The results shown in figure 9 and figure 10 indicate that spectra obtained without significant background contributions are very similar. Moreover, there is also a qualitative similarity of these data and the data shown in figure 13 for the 60° measurements on the 5.3 nm AuNP sample. Therefore, it is expected that the electron spectra of larger or smaller nanoparticles (after interaction with photons of the energies considered here) can be approximated by scaling with the interaction probability of the photons in the nanoparticles according to equation (1).

The approximation outlined in the previous paragraph should be applicable in the electron energy range above about 3 keV, that is, for Au L Auger electrons and the partially decelerated photoelectrons of the M and higher shells of gold. Within the uncertainties of the present experiment, it may also be reasonably applicable at lower electron energies, although caution should be taken when considering different coating thicknesses or materials (or even a coating plus conjugated biomolecules). A study by Morozov *et al* [56] showed a 51% suppression of low-energy electrons in the energy range below 3 keV for a PEG coating thickness of 8.5 nm. This thickness is comparatively large compared to the values reported in the review by Kuncic and Lacombe [6]. Taking the value reported by Morozov *et al* as a reference, one would roughly expect an attenuation of low-energy electrons by about 12% due to the presence of a PEG coating of 2 nm.

All of the preceding arguments apply in the case of the photon energies used in this study. The experiments reported here for only six photon energies were performed during a four-day beamtime shift. Therefore, measuring electron emission data for a wider range of photon energies is not possible given the limited availability of beamtimes at high-intensity synchrotron radiation facilities. However, photon interaction cross sections are known with uncertainties in the range of a few percent [57]. In principle, it should thus be possible to construct benchmark datasets derived from the present measurements using the XCOM photon interaction database [49]. This requires a decomposition of the measured spectra into the components that change with photon energy (photoelectrons) and those whose energy is independent of photon energy (Auger electrons). This decomposition will be the subject of the fourth part of the paper, where a detailed line shape analysis of the measured spectra will be presented.

5. Conclusions

In this work, experiments were performed on AuNP samples with a data analysis aimed at obtaining absolute results for the particle radiance of emitted electrons over a wide range of kinetic energies after photoabsorption on the L-shells of gold. To the best of our knowledge, comparable data were available in the literature only for lower energy photons after excitation of gold M-shells [58] and for irradiations with protons [52], but in both cases only on a relative scale. Experimental benchmarks of numerical methods for determining dose enhancement by high-Z materials have been performed by Alawi *et al* [22], Mirza *et al* [23] and Gray *et al* [24]. However, the respective experiments do not allow conclusions to be drawn about the energy spectra of emitted electrons as they determined the integral dosimetric effect.

The absolute determination of electron radiance proved very challenging because the major uncertainty components arise from the transmission of the electron spectrometer and the cross-sectional area of the photon beam. A photon flux monitor was used to correct for temporal changes in the photon flux and proved essential for identifying transients following changes of the photon energy. To obtain absolute values of photon flux, the photon flux monitor was calibrated. A strong variation of the calibration factor and photon flux with photon energy was found, which originated in the use of the wrong coating on the last focusing mirror. From the plausibility checks presented here and the results on the gold foil sample that will be presented in the second part of the paper, it can be ruled out that this peculiarity of the experiment impairs the results.

A major drawback of the experimental results is the non-uniform surface coverage with AuNPs and the Tougaard background of electrons produced in the sample holder. However, the fact that the emitted electron spectra were studied over large energy ranges using different samples and irradiation geometries allowed a consistent understanding of the limitations of the results.

Potential future repetitions of these experiments with the aim of producing data with lower uncertainties will need to reduce the two uncertainty contributions of global scope. For the photon beam area, this could be achieved by using a specially designed test sample that has spatial structures of about 10 μm dimensions and the possibility to study the beam in a wide range of azimuthal angles. For the electron spectrometer transmission, a reduction of uncertainty can only be reasonably achieved by electron transport simulations that take into account the details of the measurement geometry and the emitted electron spectra.

To obtain better quality data, more uniform samples and the efficient suppression of the Tougaard background will be essential. The samples used in the present experiments were designed to serve multiple purposes, including the possibility to perform TEM and low-energy proton measurements. Diamond plates with thicknesses in the micrometer range may be considered for future hard x-ray photoelectron spectroscopy measurements. These would be opaque to the electrons of a copper sample holder, and the photoelectron background should be smooth due to the low binding energy of electrons in carbon. The mechanical stability of such diamond plates would allow the wet chemical deposition of AuNPs in a more uniform monolayer [36]. AuNP samples with more uniform and known surface density will allow the determination of the radiance per AuNP rather than per area, eliminating the need to know the cross-sectional area of the beam and thus removing an important source of uncertainty.

In the present experiments, the instrumentation at the experimental station was used for the first time to measure electron emission spectra over the entire available energy range at higher photon excitation energies than commonly used. Optimizing the experimental sequences to mitigate the effects of transients in the photon beam on the measurements could then further reduce the experimental uncertainties, so that overall uncertainties of the determined particle radiance to values on the order of 10% seem achievable.

For the gold foil sample, some of the caveats identified for the AuNP samples are less relevant, as will be shown and further discussed in the second part of the paper. Despite these limitations, the results on the nanoparticle samples are still suited for further analysis such as benchmarking theoretical investigations and detailed line fitting analysis as in conventional XPS studies. These analyses are presented in the third and fourth parts of the paper.

Acknowledgments

Data availability statement

All data that support the findings of this study are included within the article (and any supplementary files).

Author contributions

HR: Methodology, Validation, Data Curation, Formal analysis, Supervision, Visualization, Writing - Original Draft, Writing - Review & Editing PAH: Sample Preparation, Investigation, Writing - Review & Editing AH, CS: Investigation, Writing - Review & Editing WYB: Investigation, Supervision, Writing - Review & Editing

ORCID iDs

Hans Rabus ⬤ https://orcid.org/0000-0001-7700-9845

References

[1] Mesbahi A 2010 A review on gold nanoparticles radiosensitization effect in radiation therapy of cancer *Rep Pract Oncol Radiother* **15** 176–80

[2] Jain S, Hirst D G and O'Sullivan J M 2012 Gold nanoparticles as novel agents for cancer therapy *Br. J. Radiol.* **85** 101–13

[3] Dorsey J F, Sun L, Joh D Y, Witztum A, Zaki A A, Kao G D, Alonso-Basanta M, Avery S, Tsourkas A and Hahn S M 2013 Gold nanoparticles in radiation research: Potential applications for imaging and radiosensitization *Transl. Cancer Res.* **2** 280–91

[4] Schuemann J, Berbeco R, Chithrani D B, Cho S H, Kumar R, McMahon S J, Sridhar S and Krishnan S 2016 Roadmap to clinical use of gold nanoparticles for radiation sensitization *International Journal of Radiation Oncology*Biology*Physics* **94** 189–205

[5] Cui L, Her S, Borst G R, Bristow R G, Jaffray D A and Allen C 2017 Radiosensitization by gold nanoparticles: will they ever make it to the clinic? *Radiother. Oncol.* **124** 344–56

[6] Kuncic Z and Lacombe S 2018 Nanoparticle radio-enhancement: principles, progress and application to cancer treatment *Phys. Med. Biol.* **63** 02TR01

[7] Hainfeld J F, Slatkin D N and Smilowitz H M 2004 The use of gold nanoparticles to enhance radiotherapy in mice *Phys. Med. Biol.* **49** N309–15

[8] Her S, Jaffray D A and Allen C 2017 Gold nanoparticles for applications in cancer radiotherapy: mechanisms and recent advancements *Adv. Drug Delivery Rev.* **109** 84–101

[9] Bromma K, Cicon L, Beckham W and Chithrani D B 2020 Gold nanoparticle mediated radiation response among key cell components of the tumour microenvironment for the advancement of cancer nanotechnology *Sci. Rep.* **10** 12096

[10] McMahon S *et al* 2011 Biological consequences of nanoscale energy deposition near irradiated heavy atom nanoparticles *Nat. Sci. Rep.* **1** 18

[11] McMahon S J *et al* 2011 Nanodosimetric effects of gold nanoparticles in megavoltage radiation therapy *Radiother. Oncol.* **100** 412–6

[12] Butterworth K T, McMahon S J, Currell F J and Prise K M 2012 Physical basis and biological mechanisms of gold nanoparticle radiosensitization *Nanoscale* **4** 4830–8

[13] Rabus H, Gargioni E, Li W, Nettelbeck and Villagrasa H C 2019 Determining dose enhancement factors of high-Z nanoparticles from simulations where lateral secondary particle disequilibrium exists *Phys. Med. Biol.* **64** 155016

[14] Rabus H, Gargioni E, Li W B, Nettelbeck H and Villagrasa C 2020 Corrigendum: Determining dose enhancement factors of high-Z nanoparticles from simulations where lateral secondary particle disequilibrium exists (2019 *Phys. Med. Biol.* 64 155016)*Phys. Med. Biol.* **65** 159501

[15] Rabus H *et al* 2021 Intercomparison of Monte Carlo calculated dose enhancement ratios for gold nanoparticles irradiated by x-rays: assessing the uncertainty and correct methodology for extended beams *Phys. Medica* **84** 241–53

[16] Moradi F, Saraee K R E, Sani S F A and Bradley D A 2021 Metallic nanoparticle radiosensitization: the role of Monte Carlo simulations towards progress *Radiat. Phys. Chem.* **180** 109294

[17] Vlastou E, Diamantopoulos S and Efstathopoulos E P 2020 Monte Carlo studies in Gold Nanoparticles enhanced radiotherapy: the impact of modelled parameters in dose enhancement *Physica Med.* **80** 57–64

[18] Li W B *et al* 2020 Intercomparison of dose enhancement ratio and secondary electron spectra for gold nanoparticles irradiated by x-rays calculated using multiple Monte Carlo simulation codes *Phys. Medica* **69** 147–63

[19] Li W B *et al* 2020 Corrigendum to 'Intercomparison of dose enhancement ratio and secondary electron spectra for gold nanoparticles irradiated by x-rays calculated using multiple Monte Carlo simulation codes [Phys. Med. 69 (2020) 147-163]*Phys. Medica* **80** 383–8

[20] Rabus H *et al* 2021 Consistency checks of results from a Monte Carlo code intercomparison for emitted electron spectra and energy deposition around a single gold nanoparticle irradiated by x-rays *Radiat. Meas.* **147** 106637

[21] Rabus H, Zankl M, Gómez-Ros J M, Villagrasa C, Eakins J, Huet C, Brkić H and Tanner R 2022 Lessons learnt from the recent EURADOS intercomparisons in computational dosimetry *Radiat. Meas.* **156** 106822

[22] Alalawi A I, Hugtenburg R P, Rahman A T A, Barry M A, Nisbet A, Alzimami K S and Bradley D A 2014 Measurement of dose enhancement close to high atomic number media using optical fibre thermoluminescence dosimeters *Radiat. Phys. Chem.* **95** 145–7

[23] Mirza J A, Choi K, Sung W, Jung S and Ye S-J 2019 Measuring radioenhancement by gold nanofilms: comparison with analytical calculations *Physica Med.* **68** 1–9

[24] Gray T, Bassiri N, David S, Patel D Y, Stathakis S, Kirby N and Mayer K M 2021 A detailed experimental and Monte Carlo analysis of gold nanoparticle dose enhancement using 6 MV and 18 MV external beam energies in a macroscopic scale *Appl. Radiat. Isot.* **171** 109638

[25] Dou Y *et al* 2016 Size-tuning ionization to optimize gold nanoparticles for simultaneous enhanced ct imaging and radiotherapy *ACS Nano* **10** 2536–48

[26] Berger M J, Coursey J S, Zucker M A and Chang J 2005 ESTAR, PSTAR, and ASTAR: Computer programs for calculating stopping-power and range tables for electrons, protons, and helium ions (version 1.2.3) Available at http://physics.nist.gov/Star (Gaithersburg, MD: National Institute of Standards and Technology)

[27] David S, Patel D Y, Cardona S M, Kirby N and Mayer K M 2022 Cellular uptake and cytotoxicity of PEGylated gold nanoparticles in C33A cervical cancer cells *Nano Ex.* **3** 025006

[28] Poignant F, Ipatov A, Chakchir O, Lartaud P-J, Testa É, Gervais B and Beuve M 2020 Theoretical derivation and benchmarking of cross sections for low-energy electron transport in gold *The European Physical Journal Plus* **135** 358

[29] Sakata D *et al* 2018 Geant4-DNA track-structure simulations for gold nanoparticles: the importance of electron discrete models in nanometer volumes *Med. Phys.* **45** 2230–42

[30] Sakata D, Kyriakou I, Tran H N, Bordage M-C, Rosenfeld A, Ivanchenko V, Incerti S, Emfietzoglou D and Guatelli S 2019 Electron track structure simulations in a gold nanoparticle using Geant4-DNA *Physica Med.* **63** 98–104

[31] Kim J-K, Seo S-J, Kim H-T, Kim K-H, Chung M-H, Kim K-R and Ye S-J 2012 Enhanced proton treatment in mouse tumors through proton irradiated nanoradiator effects on metallic nanoparticles *Phys. Med. Biol.* **57** 8309–23

[32] Hainfeld J F, Smilowitz H M, O'Connor M J, Dilmanian F A and Slatkin D N 2013 Gold nanoparticle imaging and radiotherapy of brain tumors in mice *Nanomedicine (London, England)* **8** 1601–9

[33] Borbinha J, de la Fuente Rosales L, Nettelbeck H, Thomas L, Hepperle P, Baek W Y, Di Maria S and Rabus H 2023 Experimental benchmark data for Monte Carlo simulated radiation effects of gold nanoparticles. Part II: comparison of measured and simulated electron spectra from gold nanofoils *Physica Scripta* **98** accb12

[34] Salvat F and Fernández-Varea J M 2019 Radial: a FORTRANsubroutine package for the solution of the radial Schrödinger and Dirac wave equations *Comput. Phys. Commun.* **240** 165–77

[35] Schlueter C *et al* 2019 The new dedicated HAXPES beamline P22 at PETRAIII *AIP Conf. Proc.* **2054** 040010

[36] Hepperle P, Baek W Y, Nettelbeck H and Rabus H 2022 Deposition of gold nanoparticles on a self-supporting carbon foil *Part & Part Syst Charact* **39** 2200136

[37] Hepperle P, Herman A, Khanbabaee B, Baek W Y, Nettelbeck H and Rabus H 2022 XPS examination of the chemical composition of PEGMUA-coated gold nanoparticles *Part & Part Syst Charact* **39** 2200070

[38] Casta R, Champeaux J-P, Moretto-Capelle P, Sence M and Cafarelli P 2015 Electron and photon emissions from gold nanoparticles irradiated by x-ray photons *J. Nanopart. Res.* **17** 3

[39] Perkins S T, Cullen D E, Chen M H, Rathkopf J, Scofield J and Hubbell J H 1991 *Tables and graphs of atomic subshell and relaxation data derived from the LLNL Evaluated Atomic Data Library (EADL), Z = 1—100* UCRL-50400-Vol.30 Lawrence Livermore National Lab. (LLNL) (https://doi.org/10.2172/1012142)

[40] Cullen D E 2018 *A Survey of Atomic Binding Energies for use in EPICS2017* IAEA-NDS-224 IAEA Vienna

[41] Cullen D E, Hubbell J H and Kissel L 1997 *EPDL97: the Evaluated Photon Data Library '97 Version* UCRL-50400-Vol.6-Rev.5 Lawrence Livermore National Lab. (LLNL) (https://doi.org/10.2172/295438)

[42] Henneken H, Scholze F and Ulm G 1999 Absolute total electron yield of Au(111) and Cu(111) surfaces *J. Electron. Spectrosc. Relat. Phenom.* **101–103** 1019–24

[43] Henneken H, Scholze F, Krumrey M and Ulm G 2000 Quantum efficiencies of gold and copper photocathodes in the VUV and x-ray range *Metrologia* **37** 485–8

[44] Henneken H, Scholze F and Ulm G 2000 Lack of proportionality of total electron yield and soft x-ray absorption coefficient *J. Appl. Phys.* **87** 257–68

[45] Hespeels F, Heuskin A C, Scifoni E, Kraemer M and Lucas S 2017 Backscattered electron emission after proton impact on carbon and gold films: experiments and simulations *Nucl. Instrum. Methods Phys. Res., Sect. B* **401** 8–17

[46] Hespeels F, Heuskin A C, Tabarrant T, Scifoni E, Kraemer M, Chêne G, Strivay D and Lucas S 2019 Backscattered electron emission after proton impact on gold nanoparticles with and without polymer shell coating *Phys. Med. Biol.* **64** 125007

[47] Tougaard S and Jørgensen B 1984 Inelastic background intensities in XPS spectra *Surf. Sci.* **143** 482–94

[48] Tougaard S 1986 Quantitative non-destructive in-depth composition information from XPS *Surf. Interface Anal.* **8** 257–60

[49] Berger M J, Hubbell J H, Seltzer S M, Chang J, Coursey J S, Sukumar D S R, Zucker and Olsen K 2010 Available at http://physics.nist.gov/xcom XCOM: Photon Cross section Database version 1.5) Gaithersburg MD: National Institute of Standards and Technology (https://doi.org/10.18434/T48G6X)

[50] Salvat F, Fernández-Varea J M and Sempau J 2006 *Penelope-2006: A Code System for Monte Carlo Simulation of Electron and Photon Transport* (Paris: OECD) NEA No. 622292-64-02301-1

[51] Spencer B F *et al* 2021 Inelastic background modelling applied to hard x-ray photoelectron spectroscopy of deeply buried layers: A comparison of synchrotron and lab-based (9.25 keV) measurements *Appl. Surf. Sci.* **541** 148635

[52] Hespeels F, Lucas S, Tabarrant T, Scifoni E, Kraemer M, Chêne G, Strivay D, Tran H N and Heuskin A C 2019 Experimental measurements validate the use of the binary encounter approximation model to accurately compute proton induced dose and radiolysis enhancement from gold nanoparticles *Phys. Med. Biol.* **64** 065014

[53] Baró J, Sempau J, Fernández-Varea J M and Salvat F 1995 PENELOPE: An algorithm for Monte Carlo simulation of the penetration and energy loss of electrons and positrons in matter *Nucl. Instrum. Methods Phys. Res., Sect. B* **100** 31–46

[54] Cooper J W 1990 Multipole corrections to the angular distribution of photoelectrons at low energies *Phys. Rev. A* **42** 6942–5

[55] Cooper J W 1992 Erratum: multipole corrections to the angular distribution of photoelectrons at low energies *Phys. Rev. A* **45** 3362–3362

[56] Morozov V N, Belousov A V, Krusanov G A, Kolyvanova M A, Chernyaev A P and Shtil A A 2018 Secondary electron spectral changes of irradiated gold nanoparticle caused By PEGylation *KEn* **3** 278

[57] Andreo P, Burns D T and Salvat F 2012 On the uncertainties of photon mass energy-absorption coefficients and their ratios for radiation dosimetry *Phys. Med. Biol.* **57** 2117–36

[58] Casta R, Champeaux J-P, Sence M, Moretto-Capelle P, Cafarelli P, Amsellem A and Sicard-Roselli C 2014 Electronic emission of radio-sensitizing gold nanoparticles under x-ray irradiation: experiment and simulations *J. Nanopart. Res.* **16** 2348